Taylor & Francis
Taylor & Francis Group

Mechanics Based Design of Structures and Machines
An International Journal

ISSN: 1539-7734 (Print) 1539-7742 (Online) Journal homepage: www.tandfonline.com/journals/lmbd20

A nonlinear model of the compaction drum: from chaotic behavior prediction to delayed feedback control

Dong Feng

To cite this article: Dong Feng (2026) A nonlinear model of the compaction drum: from chaotic behavior prediction to delayed feedback control, Mechanics Based Design of Structures and Machines, 54:1, 2719817, DOI: 10.1080/15397734.2026.2719817

To link to this article: https://doi.org/10.1080/15397734.2026.2719817

© 2026 The Author(s). Published with license by Taylor & Francis Group, LLC

Published online: 22 Aug 2026.

Submit your article to this journal

Article views: 97

View related articles

View Crossmark data

Citing articles: 3 View citing articles

Full Terms & Conditions of access and use can be found at
https://www.tandfonline.com/action/journalInformation?journalCode=lmbd20

MECHANICS BASED DESIGN OF STRUCTURES AND MACHINES
2026, VOL. 54, NO. 1, 2719817
https://doi.org/10.1080/15397734.2026.2719817

Taylor & Francis
by informa

OPEN ACCESS Check for updates

A nonlinear model of the compaction drum: from chaotic behavior prediction to delayed feedback control

Dong Feng

Faculty of Civil Engineering, RWTH Aachen University, Aachen, Germany

ABSTRACT

This article presents a nonlinear two-degree-of-freedom (2-DOF) model of the compaction drum, incorporating both nonlinear stiffness and delayed feedback (DF) control. The system exhibits rich dynamical behaviors, including periodic, quasi-periodic, and chaotic motions, depending on parameter variations. Through harmonic balance and numerical methods, the frequency response is analyzed, and the optimal damping and stiffness parameters are identified. The Melnikov method is employed to derive analytical criteria for the onset of chaos, which are validated through numerical simulations, including phase portraits, Poincaré maps, Fast Fourier Transform (FFT) spectra, and Lyapunov exponents. Furthermore, a DF control strategy is proposed to suppress chaotic vibrations and increase the threshold for chaos. Numerical results demonstrate that the controller effectively stabilizes the system and enhances its dynamic performance. This study provides both theoretical and practical insights into the prediction and control of chaotic behavior in compaction machinery.

HIGHLIGHTS

- A 2-DOF nonlinear model of the compaction drum with delayed feedback control was proposed.
- Frequency response was analyzed using both harmonic balance and numerical methods.
- Melnikov method predicted chaotic thresholds, validated by numerical simulations.
- Delayed feedback control effectively suppressed chaos and broadened the stable operating region.

ARTICLE HISTORY
Received 10 June 2026
Accepted 6 August 2026

KEYWORDS
Compaction drum model; nonlinear dynamics; Melnikov method; delayed feedback control; oscillator chaos

1. Introduction

Vibratory compaction machinery is a cornerstone of modern construction, essential for achieving high density and stability in soil and asphalt foundations (Batey 2009; Feng 2026a; Feng, Fu, and Liu 2026; Kumar Das and Sharma 2026; Wersäll, Nordfelt, and Larsson 2017). For asphalt pavements in particular, effective vibratory compaction is also crucial for promoting adequate densification and interlocking of road aggregates, which directly affects the mechanical integrity and long-term durability of the pavement structure (Feng 2025b; Feng, Guan, et al. 2026). The core of such machinery is its vibratory

CONTACT Dong Feng dong.feng@rwth-aachen.de Faculty of Civil Engineering, RWTH Aachen University, Mies-van-der-Rohe-Straße 1, 52074 Aachen, Germany.
Communicated by Raul D. S. G. Campilho.

© 2026 The Author(s). Published with license by Taylor & Francis Group, LLC
This is an Open Access article distributed under the terms of the Creative Commons Attribution License (http://creativecommons.org/licenses/by/4.0/), which permits unrestricted use, distribution, and reproduction in any medium, provided the original work is properly cited. The terms on which this article has been published allow the posting of the Accepted Manuscript in a repository by the author(s) or with their consent.

system, typically comprising an oscillator and an internally rotating eccentric block (Anderegg and Kaufmann 2004; Paulmichl, Adam, and Adam 2019; Yoo and Selig 1979). The dynamic interaction between these two components is the primary source of the compaction force. However, this very interaction, often characterized by strong nonlinearities from stiffness, damping, and inertial coupling, can lead to complex and undesirable dynamic phenomena, including bifurcations, multi-periodic orbits, and chaos (Feng 2026d; Liu et al. 2021; Lu et al. 2023). These phenomena manifest as excessive vibrations, reduced compaction efficiency, accelerated structural fatigue, and increased energy consumption (Liu et al. 2019; Steffanoni et al. 2024; Xu et al. 2020), making a deep understanding of the nonlinear dynamics inherent in the coupled oscillator–eccentric-block system paramount to optimizing design and ensuring operational reliability.

Traditional modeling approaches often simplify the vibratory system of the compaction drum to a single-degree-of-freedom (SDOF) model (Beainy, Commuri, and Zaman 2014; Feng 2025a; Pietzsch and Poppy 1992; Xu et al. 2022; Zhang et al. 2022), focusing solely on the oscillator's response. In engineering applications, this simplification can lead to noticeable prediction deviations, such as underestimating vibration amplitude near resonance (Pistrol et al. 2024) and mispredicting the operating-point shift (Koruk and Rajagopal 2024) when soil support conditions vary, which may cause suboptimal parameter tuning in field compaction. In addition, SDOF formulations often fail to capture exciter-related behaviors observed in practice, including speed-dependent excitation force attenuation (Chen et al. 2019) and stability changes induced by dynamic feedback from the drum (Rainer Massarsch and Fellenius 2005). While useful for basic analysis, such models fundamentally neglect the dynamic interplay between the oscillator and the eccentric exciter. This interaction is critical, as the motion of the eccentric block directly provides the excitation force while simultaneously being influenced by the reaction from the oscillator. Treating the oscillator and eccentric block as two independent coupled masses characterized by a two-degree-of-freedom (2-DOF) model undoubtedly enables a more precise characterization. Existing compactor models primarily focus on the coupling between the compactor frame and the compactor drum (Fang et al. 2018; Peng et al. 2024; Pistrol et al. 2023; Wu et al. 2022). However, in real-world systems, nonlinearities—such as those arising from nonlinear stiffness elements designed to isolate vibrations or from large-amplitude motions—are intrinsic and can drastically alter the system's behavior (Lu et al. 2016; Wang et al. 2021; Yu et al. 2024; Zhou et al. 2024). Accurate prediction of such nonlinear responses also relies on a reliable characterization of the underlying constitutive behavior, since different representations of inelastic deformation can lead to noticeable variations in the predicted mechanical response (Feng 2026f; Zhang and Needleman 2021a, 2021b, 2020). A comprehensive 2-DOF compactor drum model that fully incorporates these nonlinearities is therefore necessary to accurately predict and analyze the system's performance across its entire operational range.

Beyond accurate modeling, the control of the complex dynamics generated by this coupled system remains a significant challenge. The onset of chaos is particularly detrimental, leading to unpredictable and uncontrollable vibrations (Pyragas 1993; Werndl 2009). Passive control strategies, through parameter optimization of stiffness and damping, have been widely studied (Fan, Huang, and Huo 2024; Guo and Fang 2024; Hicken and Ramakrishnan 2024). While effective within a narrow operational band, their performance is inherently limited and non-adaptive. Active control strategies present a promising alternative for suppressing nonlinear oscillations and stabilizing chaos (Zhang et al., 2026; Huang et al., 2026). Related advances in active vibration and wave control, spanning flexible cables and strings as well as nonlinear beam, vehicle, and suspension systems, have demonstrated that feedback-based strategies can reshape resonance characteristics, dissipate vibration energy, and enlarge stable operating regions under complex excitation conditions (Abdelmonem 2025; Bauomy 2024, 2025; Bauomy and EL-Sayed 2025). Among these, delayed feedback (DF) control (Pyragas 1992), known for its ability to stabilize unstable periodic orbits without requiring a reference trajectory, is particularly well-suited for this application (Guo, Hu, and Ren 2022; Phohomsiri, Udwadia, and Bremen 2006; Watanabe, Prasad, and Sakai

2024; Watanabe and Prasad 2025). Its implementation only requires feeding back the system's own time-delayed states. Beyond single-mode oscillators, DF control has also been applied to multi-degree-of-freedom nonlinear systems, including nonlinear vibration absorbers and internally resonant 2-DOF structures, where appropriate combinations of feedback gain and delay can reshape the dynamic response and suppress resonant vibration (Chen et al. 2014; Zhao and Xu 2007). Recent studies have separately advanced nonlinear vibration modeling (Feng, Fu, Zheng, et al. 2026; Feng and Zheng 2026), chaos-prediction and control techniques (Feng 2026b, 2026e), and the dynamic analysis of vibratory compaction machinery (Fang et al. 2022); however, limited attention has been given to integrating these three research directions within an internally coupled compaction-drum model that simultaneously resolves exciter-induced chaos and its active suppression. Despite its proven efficacy in various chaotic systems, the application of DF control specifically to the 2-DOF coupled oscillator-eccentric-block system, with the aim of understanding its impact on the chaotic threshold and overall system stability, has not been thoroughly explored. Furthermore, in previous studies, compactors were typically coupled to the ground, making it impossible to isolate the chaotic effects caused by the oscillator and the eccentric block separately (Du 2025; Feng 2026c).

The present study aims to address these research gaps by developing a sophisticated 2-DOF nonlinear model that captures the essential dynamics of the coupled oscillator–eccentric block system within a compaction drum. Unlike conventional compactor–soil models and previously reported coupled-oscillator formulations, the proposed model isolates and explicitly represents the internal interaction between the oscillator and the eccentric block, thereby revealing exciter-induced energy transfer, resonance distortion, and transitions among periodic, quasi-periodic, and chaotic responses that cannot be resolved using a lumped SDOF representation. Beyond applying the Melnikov method in a standard form, this study derives a chaos-onset criterion for the reduced 2-DOF compaction-drum system and systematically evaluates its applicability against the full nonlinear model through quantitative threshold comparisons, error metrics, sensitivity analyses, and Lyapunov-exponent robustness tests. The DF controller is then incorporated into the same analytical framework to clarify how the control gain and delay modify the effective dissipation, shift the chaos boundary, and enlarge the stable operating region. Accordingly, the principal contributions are the development of an internally coupled nonlinear drum model, the analytical and numerical characterization of its resonance and chaos mechanisms, the quantitative assessment of the approximation-based Melnikov threshold, and the establishment of a DF strategy for chaos suppression. These results provide both new theoretical insight into coupling-driven chaos in compaction machinery and practical guidance for selecting excitation and control parameters to avoid unstable operating regimes.

The overall methodological workflow and the organization of the remaining sections are summarized in Fig. 1. The subsequent analysis proceeds from frequency-response characterization to chaos prediction and validation, then to delayed-feedback control and the final synthesis of the main findings.

2. Mathematical model of the compaction drum

In order to focus on the internal dynamic response of the drum induced by the eccentric excitation, a simplified planar formulation is adopted in this study. The drum–ground interaction and the associated contact-induced response are not included in this study, so that the roles of the oscillator–eccentric block coupling and the introduced nonlinear stiffness can be investigated in a clear and tractable setting. In this article, we propose a 2-DOF compaction drum model incorporating nonlinear stiffness and DF control (see Fig. 2). The dynamic equations of the model were established based on the following assumptions:

1. The oscillator and eccentric block were considered as lumped masses with stiffness and damping;

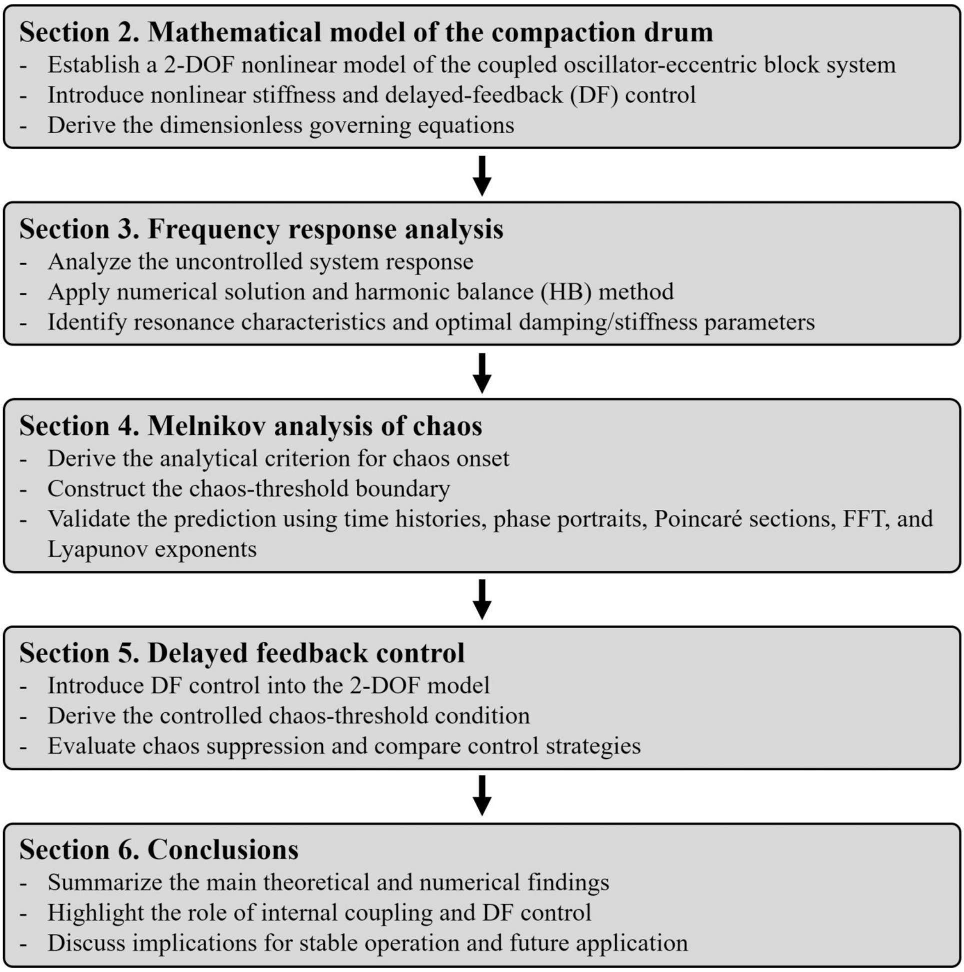

Figure 1. Roadmap of the analytical and numerical investigation.

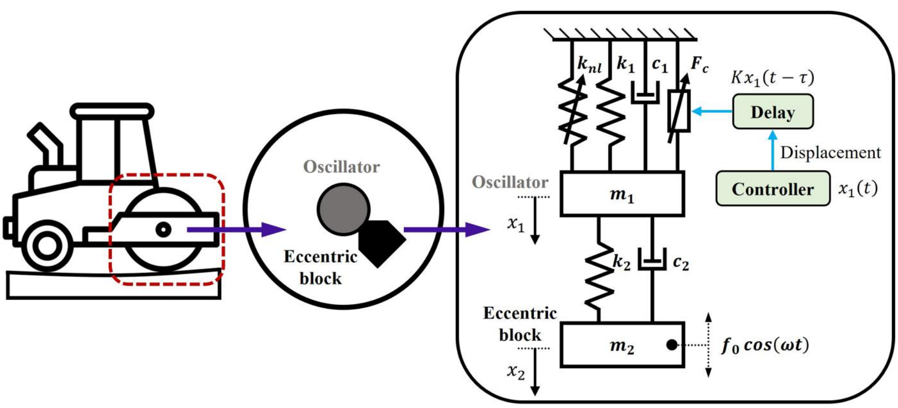

Figure 2. Two-degree-of-freedom compaction drum model.

2. All connecting elements were assumed to be massless;
3. The model was simplified to a 2D system, vibrating only in the vertical direction.

In addition, the eccentric excitation acts in a rotating manner in the plane. Since the drum–ground coupling is not considered in the present model, the dynamics of interest are governed mainly by the internal exciter-driven response rather than by any direction-specific contact constraint. Under this setting, choosing the vertical direction as the vibration coordinate is a convenient representation within the planar model, and an equivalent formulation could also be written along the horizontal direction without changing the core mechanism discussed in this study. Accordingly, the main purpose of the present work is not to reproduce the detailed drum–soil interaction or to predict the practical compaction response, but to reveal the nonlinear mechanism by which the spring-coupled drum system can generate and regulate chaotic motion. In this sense, the study is focused primarily on chaos analysis and control in a simplified theoretical model, where the essential nonlinear effect can be isolated and examined more clearly.

Let us take the static equilibrium positions of the oscillator and eccentric block as the origins of their respective coordinates, with the vertically upward direction taken as positive. The dynamic equations for the compaction drum model were as follows:

$$\begin{gathered} m_1\ddot{x}_1 + c_1\dot{x}_1 + k_1x_1 + k_{nl}x_1^3 + c_2(\dot{x}_1 - \dot{x}_2) + k_2(x_1 - x_2) + F_c = 0, \\ m_2\ddot{x}_2 + c_2(\dot{x}_2 - \dot{x}_1) + k_2(x_2 - x_1) = F_{ex}, \end{gathered} \tag{1}$$

where x_1 and x_2 are displacements of the oscillator and eccentric block, respectively. $\dot{x}_1$ and $\dot{x}_2$ are the velocities of the oscillator and eccentric block, respectively. In practical measurements, x_1 can be obtained using a linear variable differential transformer or a non-contact laser displacement sensor mounted relative to the drum frame. The velocity $\dot{x}_1$ can either be measured directly using a laser Doppler vibrometer or estimated from the sampled displacement signal through filtered numerical differentiation or a state observer. $\ddot{x}_1$ and $\ddot{x}_2$ are the accelerations of the oscillator and eccentric block, respectively. m_1 and m_2 are the masses of the oscillator and the eccentric block, respectively. k_1 and k_2 are the linear stiffness coefficients of the oscillator and eccentric block, respectively. c_1 and c_2 are the damping coefficients of the oscillator and eccentric block, respectively. k_{nl} is the nonlinear stiffness coefficient of the oscillator. $k_{nl}x_1^3$ accounts for the dominant amplitude-dependent stiffness of the oscillator-side support (e.g., mounting/isolator elements), where nonlinear behavior is most likely to occur under large-amplitude vibrations. By contrast, the oscillator–eccentric block connection is mainly a constrained mechanical linkage whose deformation is relatively small compared with the support motion, so its stiffness and damping are reasonably approximated as linear in this model. F_c is the control force, calculated as follows:

$$F_c = -Kx_1(t - \tau), \tag{2}$$

where K is the DF displacement gain, which determines the strength of the control force and can be interpreted as an equivalent active stiffness based on the delayed displacement. The time delay τ is the delay interval used to generate the feedback signal $x_1(t - \tau)$, which effectively introduces a phase shift between the control force and the oscillator motion and thus influences the vibration-suppression effect.

F_{ex} is the excitation force:

$$F_{ex} = f_0\cos(\omega t) = m_2r_e\omega^2\cos(\omega t), \tag{3}$$

where r_e and ω are the eccentric distance and rotation speed, respectively. The rotation speed was calculated as follows:

$$\omega = 2\pi f, \tag{4}$$

where f is the vibration frequency.

To facilitate analysis and numerical calculations, Equation (1) was rewritten in dimensionless form:

$$\begin{aligned}\ddot{X}_1 + 2\zeta\dot{X}_1 + sX_1 + X_1^3 + \eta\left(\dot{X}_1 - \dot{X}_2\right) + \alpha(X_1 - X_2) - \kappa_c X_1(\tau - \tilde{\tau}) = 0,\\ \gamma\ddot{X}_2 + \eta\left(\dot{X}_2 - \dot{X}_1\right) + \alpha(X_2 - X_1) = F\cos(\Omega\tau),\end{aligned} \tag{5}$$

where the dimensionless parameters are defined as follows:

$$\begin{aligned}&t = \frac{\tau}{\omega_0}, \omega_0 = \sqrt{\frac{|k_1|}{m_1}}, L = \sqrt{\frac{|k_1|}{k_{nl}}}, X_1(\tau) = \frac{x_1(t)}{L}, X_2(\tau) = \frac{x_2(t)}{L}, \zeta = \frac{c_1}{2m_1\omega_0}, \eta = \frac{c_2}{m_1\omega_0},\\ &\alpha = \frac{k_2}{|k_1|}, \gamma = \frac{m_2}{m_1}, F = \frac{f_0}{m_2 L\omega_0^2}, \Omega = \frac{\omega}{\omega_0}, \kappa_c = \frac{K}{m_1\omega_0^2}, \tilde{\tau} = \omega_0\tau, s = \mathrm{sign}(k_1),\end{aligned} \tag{6}$$

where $s = 1$ indicates positive linear stiffness, representing a single-well Duffing oscillator model primarily exhibiting hardening phenomena; $s = -1$ indicates negative linear stiffness, representing a double-well Duffing oscillator model primarily exhibiting period-doubling bifurcations and chaotic phenomena. In practical mechanical systems, an effective negative linear stiffness can arise from negative-stiffness elements or bistable mechanisms (e.g., pre-buckled structural components, magnetic negative-stiffness devices, or dedicated negative-stiffness isolator configurations), which are widely used in vibration isolation and vibration control (Le and Ahn 2011; Platus 1992; Zhu and Chai 2024). In the present study, the negative-stiffness spring is introduced to represent a class of practically used negative-stiffness or bistable elements in a simplified form. Under this setting, the model can capture the essential nonlinear restoring mechanism associated with such elements, thereby providing a suitable basis for analyzing spring-induced complex responses, including inter-well motion and chaos.

In this study, the key model parameters were selected based on widely used drum parameter sets reported in prior studies on vibratory compaction drums. Specifically, the mass, stiffness, damping, and eccentric excitation parameters were chosen to fall within the typical ranges of classic drum configurations documented in the literature (Cui et al. 2024; Feng 2025a; Lu et al. 2023), ensuring that the proposed 2-DOF model remains representative of practical engineering systems. On this basis, k_{nl} was introduced to capture the amplitude-dependent stiffness effect commonly attributed to isolators and contact-related nonlinearity in real drums, while the damping parameters were kept consistent with reported values to maintain comparable dynamic response levels.

Accordingly, the small-mass-ratio, weak-damping, and small-delay assumptions introduced in the subsequent analytical derivations can be interpreted as regime conditions rather than restrictions on the full numerical model: the eccentric-block mass must remain substantially smaller than the primary vibrating mass, the dissipative terms must be small relative to the conservative restoring forces, and the feedback delay must be short compared with the dominant vibration period. Outside these ranges, the closed-form Melnikov and small-delay approximations may lose quantitative accuracy, and the full 2-DOF ordinary differential equation (ODE) or delay differential equation (DDE) model should be used for response prediction.

In summary, this section established a dimensionless 2-DOF nonlinear model that explicitly represents the internal coupling between the oscillator and the eccentric block. The formulation incorporates nonlinear oscillator-side stiffness, linear coupling elements, eccentric excitation, and delayed displacement feedback within a unified framework. The adopted simplifications isolate the exciter-driven mechanism while retaining the essential mass, stiffness, damping, and control interactions required for the subsequent frequency-response, chaos, and control analyses. The analytical assumptions introduced later are treated as regime-specific approximations, whereas the complete ODE or DDE model remains available for numerical prediction outside these regimes.

3. Frequency response of the system

To investigate the frequency response of the 2-DOF compaction drum model, we first considered the case without DF control. Then, Equation (5) was rewritten as:

$$\begin{aligned}\ddot{X}_1+2\zeta\dot{X}_1+sX_1+X_1^3+\eta\left(\dot{X}_1-\dot{X}_2\right)+\alpha(X_1-X_2)&=0,\\ \gamma\ddot{X}_2+\eta\left(\dot{X}_2-\dot{X}_1\right)+\alpha(X_2-X_1)&=F\cos(\Omega\tau).\end{aligned} \tag{7}$$

Equation (7) cannot be solved analytically. Therefore, the numerical method and the harmonic balance (HB) method (Blondel 1919; Ginoux 2017) were employed to approximate the solution of Equation (7). First, the following state-space vector was defined for the numerical solution:

$$\boldsymbol{u}=\begin{bmatrix}u_1\\u_2\\u_3\\u_4\end{bmatrix}=\begin{bmatrix}X_1\\\dot{X}_1\\X_2\\\dot{X}_2\end{bmatrix}. \tag{8}$$

Taking the derivative of Equation (8), the dynamic system can be expressed as:

$$\dot{\boldsymbol{u}}=\boldsymbol{A}_{\boldsymbol{matrix}}\boldsymbol{u}+\boldsymbol{B}_{\boldsymbol{matrix}}(\boldsymbol{u},\tau), \tag{9}$$

where $\boldsymbol{A}_{\boldsymbol{matrix}}$ and $\boldsymbol{B}_{\boldsymbol{matrix}}(\boldsymbol{u},\tau)$ are defined as follows:

$$\begin{aligned}\boldsymbol{A}_{\boldsymbol{matrix}}&=\begin{bmatrix}0&1&0&0\\-(s+\alpha)&-(2\zeta+\eta)&\alpha&\eta\\0&0&0&1\\\dfrac{\alpha}{\gamma}&\dfrac{\eta}{\gamma}&-\dfrac{\alpha}{\gamma}&-\dfrac{\eta}{\gamma}\end{bmatrix},\\ \boldsymbol{B}_{\boldsymbol{matrix}}(\boldsymbol{u},\tau)&=\begin{bmatrix}0\\-u_1^3\\0\\\dfrac{F}{\gamma}\cos(\Omega\tau)\end{bmatrix}.\end{aligned} \tag{10}$$

In this study, the ode45 (Dormand and Prince 1980; Shampine and Reichelt 1997) function in MATLAB was employed to numerically solve the system of ODEs depicted in Equation (10). In the frequency-response calculations, the relative and absolute error tolerances were set to 10^{-6} and 10^{-8}, respectively, and the maximum step size was limited to 0.1 in dimensionless time; 2000 equally spaced output times were requested for each frequency point. For the long-time nonlinear-response, chaos-diagnostic, model-comparison, and instantaneous-feedback calculations, stricter settings of $\mathrm{RelTol}=10^{-8}$ and $\mathrm{AbsTol}=10^{-9}$ were adopted, with $\mathrm{MaxStep}=0.5T_\Omega=\pi/\Omega$, where $T_\Omega=2\pi/\Omega$ is the excitation period. All other ode45 options retained their MATLAB default values. The initial conditions for this system are as follows:

$$X_1|_{\tau=0}=0,\dot{X}_1|_{\tau=0}=0,X_2|_{\tau=0}=0,\dot{X}_2|_{\tau=0}=0. \tag{11}$$

In addition, the HB method was used to analytically approximate the solution of Equation (7). Assuming that the system responds at the fundamental frequency Ω, the harmonic solutions are taken as follows:

$$\begin{aligned}X_1&=A\cos(\Omega\tau+\phi)=\mathrm{Re}\left[\tilde{X}_1e^{i\Omega\tau}\right],\tilde{X}_1=Ae^{i\phi},\\ X_2&=B\cos(\Omega\tau+\psi)=\mathrm{Re}\left[\tilde{X}_2e^{i\Omega\tau}\right],\tilde{X}_2=Be^{i\psi},\end{aligned} \tag{12}$$

where A and B represent the dimensionless displacement amplitudes of X_1 and X_2, and ϕ and ψ are the corresponding phase angles.

Due to the presence of the nonlinear term X_1^3 (see Equation (7)), it is necessary to approximate it using fundamental frequency harmonics. In this study, we only considered a first-order approximation, thus neglecting higher harmonics (i.e., considering only the fundamental frequency component). Therefore, we approximate the nonlinear term as:

$$X_1^3 \approx \frac{3}{4}A^2 A\cos(\Omega\tau + \phi) = \frac{3}{4}\left|\tilde{X}_1\right|^2 \tilde{X}_1 e^{i\Omega\tau}. \tag{13}$$

Substituting Equations (12) and (13) into Equation (7), we obtain:

$$\begin{gathered}\left(-\Omega^2 + i\Omega(2\zeta + \eta) + (s + \alpha) + \frac{3}{4}\left|\tilde{X}_1\right|^2\right)\tilde{X}_1 - (i\Omega\eta + \alpha)\tilde{X}_2 = 0, \\ -(i\Omega\eta + \alpha)\tilde{X}_1 + \left(-\gamma\Omega^2 + i\Omega\eta + \alpha\right)\tilde{X}_2 = F.\end{gathered} \tag{14}$$

Converting Equation (14) into matrix form, we obtain:

$$\begin{bmatrix} D_{\tilde{X}_1}(\Omega, A) & -D_{\tilde{X}_1\tilde{X}_2} \\ -D_{\tilde{X}_1\tilde{X}_2} & D_{\tilde{X}_2}(\Omega) \end{bmatrix} \begin{bmatrix} \tilde{X}_1 \\ \tilde{X}_2 \end{bmatrix} = \begin{bmatrix} 0 \\ F \end{bmatrix}. \tag{15}$$

where:

$$\begin{gathered} D_{\tilde{X}_1}(\Omega, A) = -\Omega^2 + i\Omega(2\zeta + \eta) + (s + \alpha) + \frac{3}{4}A^2, \\ D_{\tilde{X}_1\tilde{X}_2} = i\Omega\eta + \alpha, \\ D_{\tilde{X}_2}(\Omega) = -\gamma\Omega^2 + i\Omega\eta + \alpha, \\ A = \left|\tilde{X}_1\right|. \end{gathered} \tag{16}$$

Solving Equation (15), we obtain:

$$\begin{gathered} A = \left|\tilde{X}_1\right| = \left|\frac{D_{\tilde{X}_1\tilde{X}_2}F}{D_{\tilde{X}_1}(\Omega, A)D_{\tilde{X}_2}(\Omega) - D^2_{\tilde{X}_1\tilde{X}_2}}\right|, \\ \tilde{X}_2 = \frac{F}{D_{\tilde{X}_2}(\Omega) - \frac{D^2_{\tilde{X}_1\tilde{X}_2}}{D_{\tilde{X}_1}(\Omega, A)}}. \end{gathered} \tag{17}$$

By solving Equation (7) using the adaptive ode45 method and the HB method, respectively, and considering two different combinations of damping parameters, the amplitude-frequency curves shown in Fig. 3 were obtained. As illustrated, both the numerical solution and the analytical approximation exhibited a periodic growth trend. The numerical discrepancy between the two remained within 1%, indicating good consistency between their results.

To better interpret the resonance features in Fig. 3, the two natural frequencies of the corresponding linearized 2-DOF system were computed by linearizing Equation (7) around the equilibrium and neglecting the nonlinear stiffness term. As expected, two modal frequencies exist. For the present parameter sets with a small mass ratio ($\gamma = 0.01$), the higher natural frequency is mainly associated with the local relative motion of the eccentric block and lies far above the practical excitation range considered here. Therefore, only the lower, physically relevant natural frequency is reported and marked in Fig. 3 ($\Omega_n = 1.407$ in (a) and $\Omega_n = 1.379$ in (b)). As shown in Fig. 3, the system response is dominated by a pronounced resonance region near Ω_n. The steep peak and the sudden amplitude change indicate a typical nonlinear resonance feature with jump behavior, implying the coexistence of multiple steady responses in a narrow frequency band. Comparing panels (a) and (b), the larger damping level leads to a smoother response and a

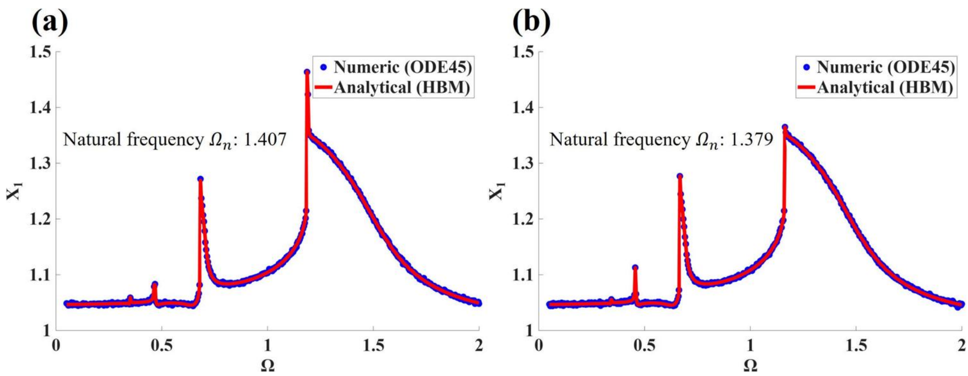

Figure 3. System frequency response curve for (a) $s = -1, \zeta = 2 \times 10^{-3}, \eta = 0.02, \gamma = 0.01, F = 0.1, \alpha = 1$, (b) $s = -1, \zeta = 2 \times 10^{-3}$, $\eta = 0.04, \gamma = 0.01, F = 0.1, \alpha = 5$.

reduced peak magnitude, which is consistent with enhanced energy dissipation and improved suppression of large-amplitude vibrations.

To provide a theoretical baseline for parameter selection and to interpret the resonance-mitigation mechanism, we further relate the present 2-DOF configuration to the classical tuned-mass-damper setting. In the small-response regime (or equivalently, by linearizing Equation (7) around the equilibrium and temporarily neglecting the nonlinear stiffness term), the eccentric block behaves as an attached absorber mass, and the pair (α, η) plays the role of stiffness and damping tuning parameters that shape the resonance peaks of the primary oscillator. Therefore, Den Hartog's theory (Hartog 2013) is introduced here as a practical and widely accepted guideline to estimate near-optimal tuning values, which are then used as reference values (initial design points) for the subsequent nonlinear analysis. According to Den Hartog's theory (Hartog 2013), a displacement-based peak method can also be used to approximate the optimal stiffness and damping parameters for Equation (7). The optimal stiffness ratio (i.e., equivalent resonance matching) is:

$$\alpha_{opt} \approx \frac{1}{1+\gamma}. \tag{18}$$

The optimal damping ratio is:

$$\eta_{opt} \approx \sqrt{\frac{3\gamma}{8(1+\gamma)}}. \tag{19}$$

We considered the cases where $\gamma = 0.01$ and $\gamma = 0.05$. These values correspond to a small mass-ratio regime, which is physically reasonable for compaction drum systems where the eccentric block typically acts as an internal exciter with a mass much smaller than that of the primary drum-related vibrating structure. Therefore, adopting $\gamma \ll 1$ is not only convenient for analytical treatment, but also consistent with the engineering role of the eccentric block as a secondary subsystem that perturbs, rather than dominates, the overall drum vibration.

For $\gamma = 0.01$, the theoretically optimal parameters are:

$$\begin{aligned} \alpha_{opt} &\approx \frac{1}{1+0.01} \approx 0.990, \\ \eta_{opt} &\approx \sqrt{\frac{3 \cdot 0.01}{8(1+0.01)}} = 0.061. \end{aligned} \tag{20}$$

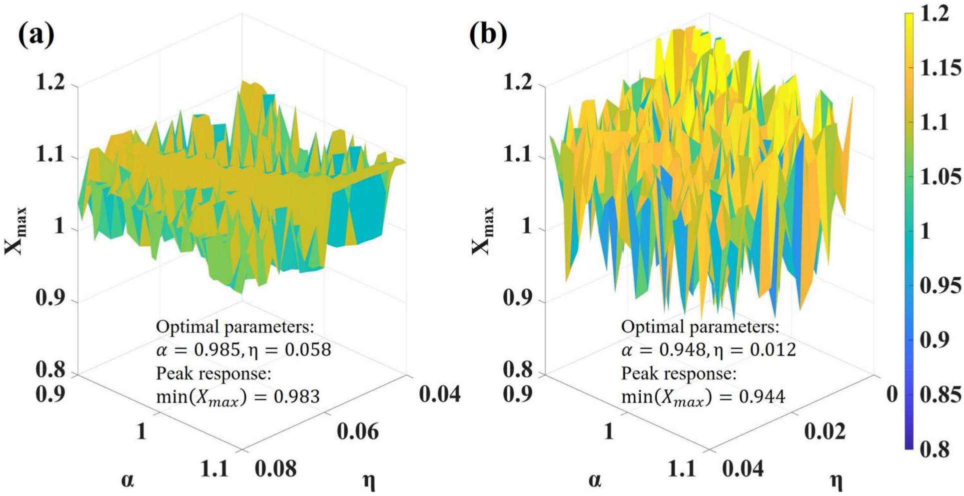

Figure 4. Influence of different mass ratios γ on optimal parameters based on $\Omega = 0.3, s = -1, \zeta = 2 \times 10^{-3}, F = 0.1$: (a) $\gamma = 0.01$, (b) $\gamma = 0.05$.

For $\gamma = 0.05$, the theoretically optimal parameters are:

$$\alpha_{opt} \approx \frac{1}{1 + 0.05} \approx 0.952, \quad \eta_{opt} \approx \sqrt{\frac{3 \cdot 0.05}{8(1 + 0.05)}} = 0.134. \tag{21}$$

Furthermore, a scan of different parameter combinations was performed to obtain the maximum amplitude at steady state, with the results shown in Fig. 4. For the two cases, the minimum values of $X_{\max}$ were 0.983 and 0.944, respectively, with the corresponding (α, η) values being (0.985, 0.058) and (0.948, 0.012), respectively. Compared with the theoretically optimal parameter combination, the parameter combination obtained through parameter scanning exhibited slight differences, though these remained within acceptable ranges. Quantitatively, for $\gamma = 0.01$, the deviations in α and η are about 0.5% and 4.9%, respectively, while for $\gamma = 0.05$, the deviation in α remains small (about 0.4%) but the deviation in η becomes much more pronounced. This indicates that the optimal stiffness is relatively robust to nonlinear effects, whereas the optimal damping is more sensitive to amplitude-dependent resonance shift and distortion of the frequency–amplitude response, which are not captured by the classical linear Den Hartog theory. This is attributed to the shift in resonance peak positions (frequency deviation, distortion in the frequency-amplitude response, etc.) when Den Hartog's optimal tuning conditions are applied to nonlinear systems. Consequently, the optimal parameter combination derived from numerical simulations differs from the theoretical values.

In summary, the frequency-response analysis demonstrates that the coupled system exhibits pronounced nonlinear resonance and jump behavior near its lower natural frequency. The close agreement between the HB and numerical solutions supports the accuracy of the fundamental-harmonic approximation for the investigated conditions, while increased damping reduces and smooths the resonance peak. The comparison between Den Hartog's estimates and the parameter-scan results further shows that the near-optimal stiffness remains relatively robust, whereas the damping optimum is more sensitive to nonlinear resonance distortion. These findings provide the passive parameter basis for the subsequent investigation of chaos onset.

4. Melnikov analysis of chaos

To further investigate the nonlinear behavior of the system, particularly the onset of complex dynamics, the Melnikov method (Melnikov 1963) is adopted. By evaluating the Melnikov function, this method provides an analytical criterion for the transverse intersection of the stable and unstable manifolds associated with the perturbed homoclinic orbit. Such an intersection indicates the occurrence of homoclinic tangles and chaotic dynamics; therefore, the Melnikov approach is widely used to estimate the critical parameter threshold for the onset of chaos. In this study, the Melnikov criterion is employed to derive an analytical prediction of the chaos threshold, which is then used as a theoretical reference for the subsequent numerical analysis and control design.

To apply the Melnikov method, we decompose the system into two parts: a main system that is conservative and can be written in Hamiltonian form, and a small perturbation that includes damping, coupling, and external forcing. For this purpose, we introduced a small parameter ε and assumed the damping to be small:

$$\begin{aligned} 2\zeta &= \varepsilon\tilde{\zeta}, \\ \eta &= \varepsilon\tilde{\eta}. \end{aligned} \tag{22}$$

Substituting Equation (22) into Equation (7), we obtain:

$$\begin{aligned} \ddot{X}_1 + sX_1 + X_1^3 + \alpha(X_1 - X_2) &= -\varepsilon\left(\tilde{\zeta}\dot{X}_1 + \tilde{\eta}\left(\dot{X}_1 - \dot{X}_2\right)\right), \\ \gamma\ddot{X}_2 + \alpha(X_2 - X_1) &= F\cos(\Omega\tau) - \varepsilon\tilde{\eta}\left(\dot{X}_2 - \dot{X}_1\right). \end{aligned} \tag{23}$$

When $\varepsilon = 0$, Equation (23) is:

$$\begin{aligned} \ddot{X}_1 + sX_1 + X_1^3 + \alpha(X_1 - X_2) &= 0, \\ \gamma\ddot{X}_2 + \alpha(X_2 - X_1) &= F\cos(\Omega\tau). \end{aligned} \tag{24}$$

This is a forced 2-DOF nonlinear Hamiltonian system, whose Hamiltonian can be expressed as:

$$\boldsymbol{H}(\boldsymbol{Z}, \tau) = \frac{1}{2}\dot{X}_1^2 + \frac{\gamma}{2}\dot{X}_2^2 + \frac{s}{2}X_1^2 + \frac{1}{4}X_1^4 + \frac{\alpha}{2}(X_1 - X_2)^2 - FX_2\cos(\Omega\tau), \tag{25}$$

where $\boldsymbol{Z} = \left(X_1, \dot{X}_1, X_2, \dot{X}_2\right)$.

It should be noted that this weak-coupling reduction is introduced only to derive a tractable analytical criterion within the Melnikov framework. The full coupled 2-DOF dynamics, including strong coupling effects, are still investigated numerically in the subsequent sections, where the analytical result serves as a reference. To obtain a tractable reduced form for qualitative analysis, we adopt the physically motivated assumption that the coupling stiffness α is sufficiently small compared with the primary oscillator stiffness level (i.e., $\alpha \ll 1$ in the nondimensional form). This corresponds to a weak-coupling regime in which the interaction between the oscillator and the eccentric block introduces only a higher-order correction to the intrinsic nonlinear oscillation of X_1. From an engineering perspective, this assumption is reasonable when the internal exciter mainly acts as a secondary subsystem that perturbs, rather than dominates, the global vibration of the drum. In this sense, the weak-coupling condition is adopted here as an analytical idealization for identifying the onset of complex dynamics, while the engineering behavior of the actual system is further evaluated through the full numerical model. Under this weak-coupling approximation, the leading-order dynamics of the oscillator can be obtained by neglecting the coupling term $\alpha(X_1 - X_2)$ in the first equation of Equation (24), yielding the simplified autonomous Duffing equation in Equation (26) for the double-well case ($s = -1$):

$$\ddot{X}_1 - X_1 + X_1^3 = 0. \tag{26}$$

Multiplying Equation (26) by $\dot{X}_1$ and integrating yields:

$$\dot{X}_1\ddot{X}_1 - \dot{X}_1 X_1 + \dot{X}_1 X_1^3 = 0 \Longrightarrow \frac{\mathrm{d}}{\mathrm{d}t}\left(\frac{1}{2}\dot{X}_1^2 - \frac{1}{2}X_1^2 + \frac{1}{4}X_1^4\right) = 0. \tag{27}$$

Thus, there exists an integration constant C such that:

$$\frac{1}{2}\dot{X}_1^2 - \frac{1}{2}X_1^2 + \frac{1}{4}X_1^4 = C. \tag{28}$$

For the homoclinic orbit connecting to the saddle point $X_1 = 0$ (where $X_1 \to 0$ as $\tau \to \pm\infty$ so that $\dot{X}_1 \to 0$), substituting into the left and right limits yields the constant $C = 0$. Then, we have:

$$\frac{1}{2}\dot{X}_1^2 = \frac{1}{2}X_1^2 - \frac{1}{4}X_1^4 \Longrightarrow \dot{X}_1^2 = X_1^2\left(1 - \frac{X_1^2}{2}\right). \tag{29}$$

Separating variables and solving for $X_1(\tau)$ yields the positive branch (the other branch is obtained by sign transformation), resulting in:

$$\frac{\mathrm{d}X_1}{X_1\sqrt{1-\frac{X_1^2}{2}}} = \pm\mathrm{d}\tau. \tag{30}$$

Integrating Equation (30) yields the standard solution:

$$\begin{aligned} X_1(\tau) &= \pm\sqrt{2}\mathrm{sech}(\tau-\tau_0), \\ \dot{X}_1(\tau) &= \mp\sqrt{2}\mathrm{sech}(\tau-\tau_0)\tanh(\tau-\tau_0), \end{aligned} \tag{31}$$

where τ_0 is an arbitrary phase (time) shift of the homoclinic orbit.

For a dynamical system with 2-DOF that is non-autonomous (see Equation (24)), a strictly analytical homogeneous solution does not exist. However, we can express X_2 in terms of Green's functions to obtain a non-local action on X_1. Treating the eccentric block equation in Equation (24) as a linear equation with constant coefficients in X_2 and letting the forcing term be $\alpha X_1 + F\cos(\Omega\tau)$, we have:

$$\gamma\ddot{X}_2 + \alpha X_2 = \alpha X_1 + F\cos(\Omega\tau). \tag{32}$$

Let $\Omega_n^2 = \frac{\alpha}{\gamma}$ (coupling-mass natural angular frequency), then the frequency of the homogeneous solution is Ω_n. Under the stability boundary conditions (assuming the existence of a definite solution such that a steady-state solution without residual terms exists), the causal Green's function $G(\tau)$ is given by:

$$G(\tau) = \frac{1}{\gamma\Omega_n}\sin(\Omega_n\tau). \tag{33}$$

For the linear operator $\mathcal{L}_2 = \gamma d^2/d\tau^2 + \alpha$, the solution of Equation (32) can be written as the sum of the homogeneous response and the convolution of the Green's function with the forcing term:

$$X_2(\tau) = X_{2,h}(\tau) + \int_{-\infty}^{\tau} G(\tau - s)\left[\alpha X_1(s) + F\cos(\Omega s)\right]\mathrm{d}s. \tag{34}$$

The homogeneous component is $X_{2,h} = C_1\cos(\Omega_n\tau) + C_2\sin(\Omega_n\tau)$. Because the bounded steady-state response is considered, the residual free-oscillation component is omitted. For $\Omega \neq \Omega_n$, the harmonic part of the convolution satisfies:

$$F\int_{-\infty}^{\tau} G(\tau-s)\cos(\Omega s)\mathrm{d}s = \frac{F}{\gamma\left(\Omega_n^2-\Omega^2\right)}\cos(\Omega\tau). \tag{35}$$

Then, the forced solution, obtained from the steady-state Green's-function convolution without free-oscillation components, is:

$$X_2(\tau) = \frac{\alpha}{\gamma\Omega_n}\int_{-\infty}^{\tau}\sin(\Omega_n(\tau-s))X_1(s)\mathrm{d}s + \frac{F}{\gamma\left(\Omega_n^2-\Omega^2\right)}\cos(\Omega\tau). \tag{36}$$

The coupling term in the first equation of Equation (24) therefore becomes:

$$\alpha(X_1-X_2) = \alpha X_1 - \frac{\alpha^2}{\gamma\Omega_n}\int_{-\infty}^{\tau}\sin(\Omega_n(\tau-s))X_1(s)\mathrm{d}s - \frac{\alpha F}{\gamma\left(\Omega_n^2-\Omega^2\right)}\cos(\Omega\tau). \tag{37}$$

The integral term represents the history-dependent reaction of the eccentric block on the oscillator, whereas the final term is the transmitted harmonic excitation. Substituting this expression into the first equation of Equation (24) yields the following:

$$\begin{gathered}\ddot{X}_1 + (s+\alpha)X_1 + X_1^3, \\ -\alpha\left(\frac{\alpha}{\gamma\Omega_n}\int_{-\infty}^{\tau}\sin(\Omega_n(\tau-s))X_1(s)\mathrm{d}s + \frac{F}{\gamma\left(\Omega_n^2-\Omega^2\right)}\cos(\Omega\tau)\right) = 0.\end{gathered} \tag{38}$$

Thus, the original 2-DOF coupling problem is equivalently transformed into a single-unknown nonlocal equation. However, Equation (38) does not possess an analytical closed-form solution. Nevertheless, this formulation can be further solved using theoretical approximations (such as high-frequency/low-frequency limit expansions) and numerical methods.

When $0<\varepsilon\ll 1$, the damping term is considered (see Equation (23)). When the stiffness term α is sufficiently small or the damping terms $\tilde{\zeta}$ and $\tilde{\eta}$ are sufficiently large, the original system can be regarded as weakly coupled, thereby converting the 2-DOF problem into a 1-DOF problem. However, for a realistic compaction drum model, the above assumptions are overly idealized. Therefore, we considered the more general strongly coupled case. For the perturbation term in Equation (23), expressed in vector field form:

$$\boldsymbol{g}(\boldsymbol{Z}) = \begin{pmatrix} 0 \\ -\tilde{\zeta}\dot{X}_1 - \tilde{\eta}\left(\dot{X}_1-\dot{X}_2\right) \\ 0 \\ -\dfrac{\tilde{\eta}}{\gamma}\left(\dot{X}_2-\dot{X}_1\right)\end{pmatrix}. \tag{39}$$

Then, the dynamical system is given as follows:

$$\dot{\boldsymbol{Z}} = J\nabla\boldsymbol{H}(\boldsymbol{Z},\tau) + \varepsilon\boldsymbol{g}(\boldsymbol{Z}), \tag{40}$$

where J is the standard 4×4 symplectic matrix corresponding to the 2-DOF Hamiltonian system (i.e., $Z\in\mathbb{R}^4$).

Since the main system is non-autonomous (periodic), we cannot directly apply the standard Melnikov criterion for a single saddle point. Instead, we seek a saddle-periodic construction: namely, the main system ($\varepsilon=0$) possesses a hyperbolic periodic solution $P(\tau)$ (period $T=2\pi/\Omega$), and there exists a trajectory $\boldsymbol{Z}(\tau)$ in the extended space that is homoclinic to this periodic orbit (asymptotic to it as $\tau\to\pm\infty$). In this case, for a 2-DOF system, the Melnikov function measures the distance between stable and unstable manifolds under first-order perturbations, expressed as:

$$M(\tau_0) = \int_{-\infty}^{\infty} \nabla \boldsymbol{H}(\boldsymbol{Z}, \tau) \cdot \boldsymbol{g}(\boldsymbol{Z}) \mathrm{d}\tau, \tag{41}$$

where τ_0 is the relative phase between the perturbation and the unperturbed homoclinic (to-periodic-orbit) trajectory, and

$$\nabla \boldsymbol{H}(\boldsymbol{Z}, \tau) = \begin{bmatrix} \dfrac{\partial \boldsymbol{H}}{\partial X_1} \\ \dfrac{\partial \boldsymbol{H}}{\partial \dot{X}_1} \\ \dfrac{\partial \boldsymbol{H}}{\partial X_2} \\ \dfrac{\partial \boldsymbol{H}}{\partial \dot{X}_2} \end{bmatrix} = \begin{bmatrix} sX_1 + X_1^3 + \alpha(X_1 - X_2) \\ \dot{X}_1 \\ \alpha(X_2 - X_1) - F\cos(\Omega\tau) \\ \gamma \dot{X}_2 \end{bmatrix}. \tag{42}$$

For the dot product of the Hamiltonian gradient and the perturbation vector (see Equation (41)), only the velocity term contributes to damping. Therefore, we have:

$$M(\tau_0) = \int_{-\infty}^{\infty} \left[\dot{X}_1 \left(-\tilde{\zeta} \dot{X}_1 - \tilde{\eta} \left(\dot{X}_1 - \dot{X}_2 \right) \right) + \gamma \dot{X}_2 \left(-\frac{\tilde{\eta}}{\gamma} \left(\dot{X}_2 - \dot{X}_1 \right) \right) \right] \mathrm{d}\tau. \tag{43}$$

Simplifying Equation (43) yields the Melnikov function expression under damped-coupled perturbations:

$$M(\tau_0) = -\int_{-\infty}^{\infty} \left[\tilde{\zeta} \dot{X}_1^2 + \tilde{\eta} \left(\dot{X}_1 - \dot{X}_2 \right)^2 \right] \mathrm{d}\tau. \tag{44}$$

For Equation (44), a sign change (simple zero) of $M(\tau_0)$ indicates transverse intersection, and the system may transition from homoclinic orbits to chaos. However, Equation (44) exhibits coupling between X_1 and X_2. Therefore, a reasonable assumption is required to achieve decoupling.

To proceed with an explicit Melnikov integral, we introduce an additional approximation based on a small mass ratio. This assumption is consistent with many practical drum–eccentric block configurations where the eccentric block mass is much smaller than the oscillator mass, and it enables an analytical closed-form threshold. The validity of the resulting criterion is assessed by comparison with numerical results of the full 2-DOF model presented later. When $\gamma \ll 1$, the mass of the eccentric block is much smaller than that of the oscillator, meaning X_2 follows X_1. Therefore, for the second expression in Equation (24), the following approximation holds:

$$X_2 \approx X_1 + \frac{F}{\alpha} \cos(\Omega\tau). \tag{45}$$

Equation (45) follows from the leading-order balance of the second equation of Equation (24). Specifically, when $\gamma \ll 1$, the inertial contribution $\gamma \ddot{X}_2$ is of higher order, and the remaining algebraic balance gives:

$$\alpha(X_2 - X_1) = F\cos(\Omega\tau) + O(\gamma), \tag{46}$$

from which Equation (45) is obtained. This quasi-static approximation is used only to derive the closed-form first-order threshold, while the inertia and full coupling of the eccentric block are retained in the subsequent numerical simulations.

Then, substituting Equation (45) into the first expression of Equation (23) yields:

$$\ddot{X}_1 + sX_1 + X_1^3 = F\cos(\Omega\tau) - \varepsilon(\tilde{\zeta} + \tilde{\eta})\dot{X}_1. \tag{47}$$

The resulting critical excitation is given by (see Appendix A):

$$F_{critical}(\Omega) = \frac{2\sqrt{2}}{3\pi}|s|^{\frac{3}{2}}(\tilde{\zeta} + \tilde{\eta})\operatorname{sech}^{-1}\left(\frac{\pi\Omega}{2\sqrt{|s|}}\right). \tag{48}$$

As shown in Fig. 5, the analytical critical boundary predicted by the Melnikov criterion is plotted in the (Ω, F) plane. This boundary provides a threshold indication for the onset of complex non-periodic responses associated with transverse intersections of invariant manifolds in the perturbed system. The curve divides the parameter plane into two qualitatively different regimes: when the excitation level lies below the critical line (region A), the system response remains periodic for the considered conditions; when the excitation level approaches or exceeds the line (regions B and C), the response tends to become non-periodic and more sensitive to small variations in parameters and initial states, which is consistent with the emergence of manifold tangling near the transition. In addition, the overall trend of the boundary shows that lower excitation frequencies require higher excitation amplitudes to trigger the transition, whereas at higher frequencies the critical excitation decreases and gradually levels off, reflecting the frequency-dependent balance between energy input from excitation and dissipation in the system.

To validate Equation (48), we selected three points corresponding to A, B, and C in Fig. 5 for dynamic response analysis. For each case, we plotted displacement-time diagrams, velocity-time diagrams, phase portraits, Poincaré section diagrams, Fast Fourier Transform (FFT) spectrum plots, and Lyapunov exponent diagrams. Figures 6–8 correspond to the results for cases A, B, and C, respectively.

A. The oscillator exhibited a regular periodic response: the phase portrait formed a single closed loop, and the stroboscopic Poincaré section collapsed into a compact set of discrete points (appearing as a short arc due to the finite phase tolerance and numerical sampling). The FFT spectrum was dominated by the driving frequency and its harmonics rather than a

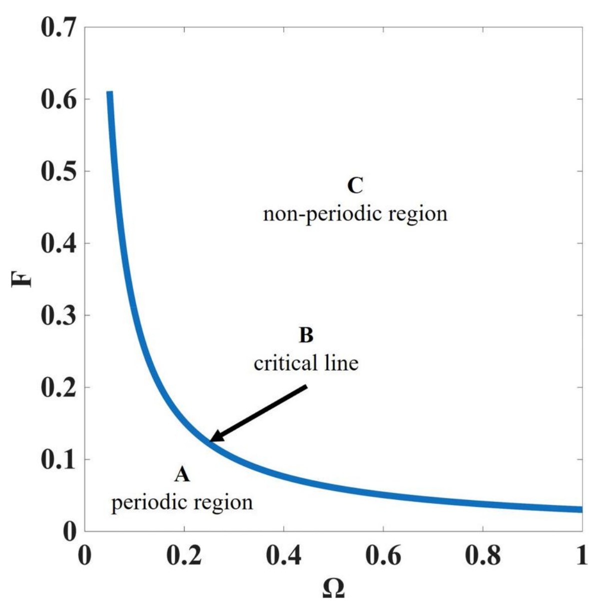

Figure 5. Influence of initial values on homoclinic orbits based on parameters $s = -1, \zeta = 2 \times 10^{-3}, \eta = 0.02, \gamma = 0.01, \alpha = 1$.

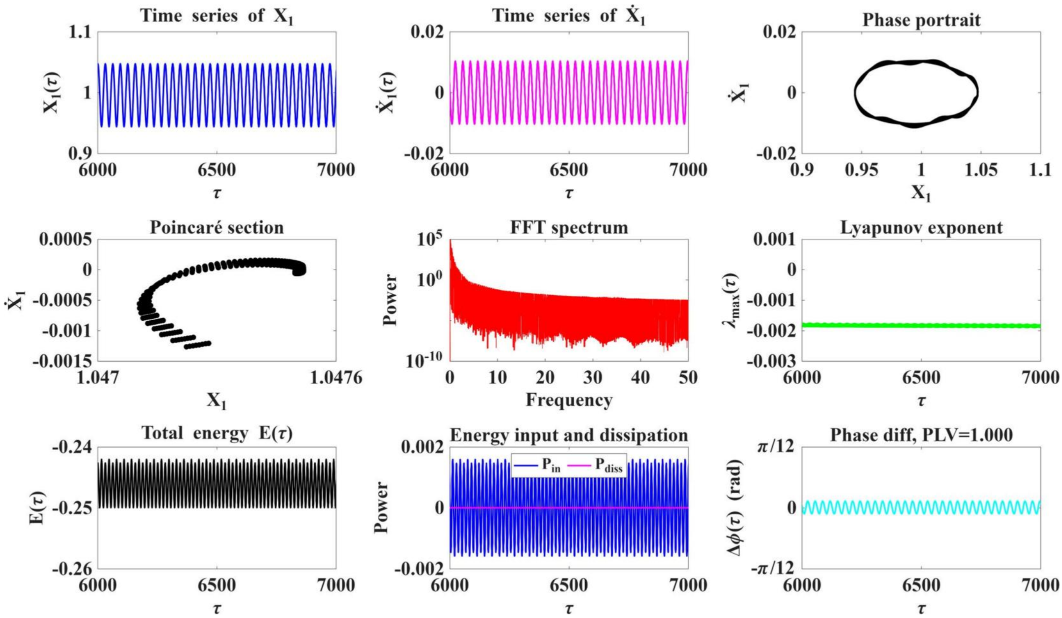

Figure 6. System response results based on parameters $s = -1, \zeta = 2 \times 10^{-3}, \eta = 0.02, \gamma = 0.01, \alpha = 1, \Omega = 0.2, F = 0.1$.

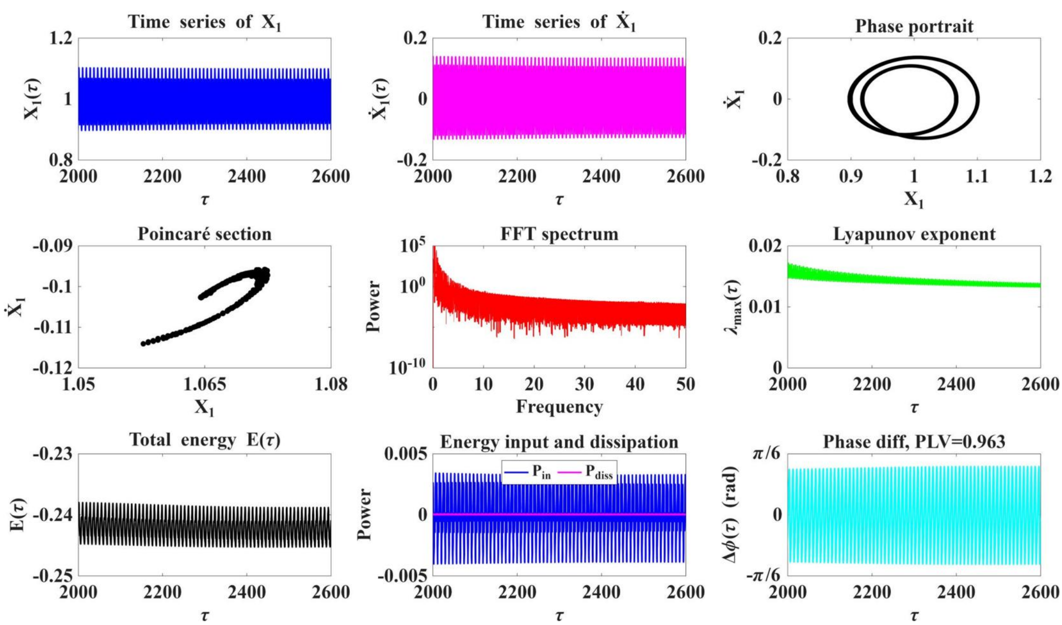

Figure 7. System response results based on parameters $s = -1, \zeta = 2 \times 10^{-3}, \eta = 0.02, \gamma = 0.01, \alpha = 1, \Omega = 0.7, F = 0.03$.

continuous broadband component. Moreover, the largest Lyapunov exponent (LLE) remained negative and its running estimate converged with time, which is consistent with an asymptotically stable periodic motion in this regime. From a physical-mechanism viewpoint, the total mechanical energy $E(\tau)$ stayed bounded and oscillated in a highly regular manner. The injected power $P_{in}(\tau)$ and dissipated power $P_{diss}(\tau)$ showed a repeatable cycle-to-cycle balance, indicating that the excitation energy was continuously compensated by dissipation without cumulative energy growth. Meanwhile, the phase difference $\Delta\phi(\tau)$ remained nearly

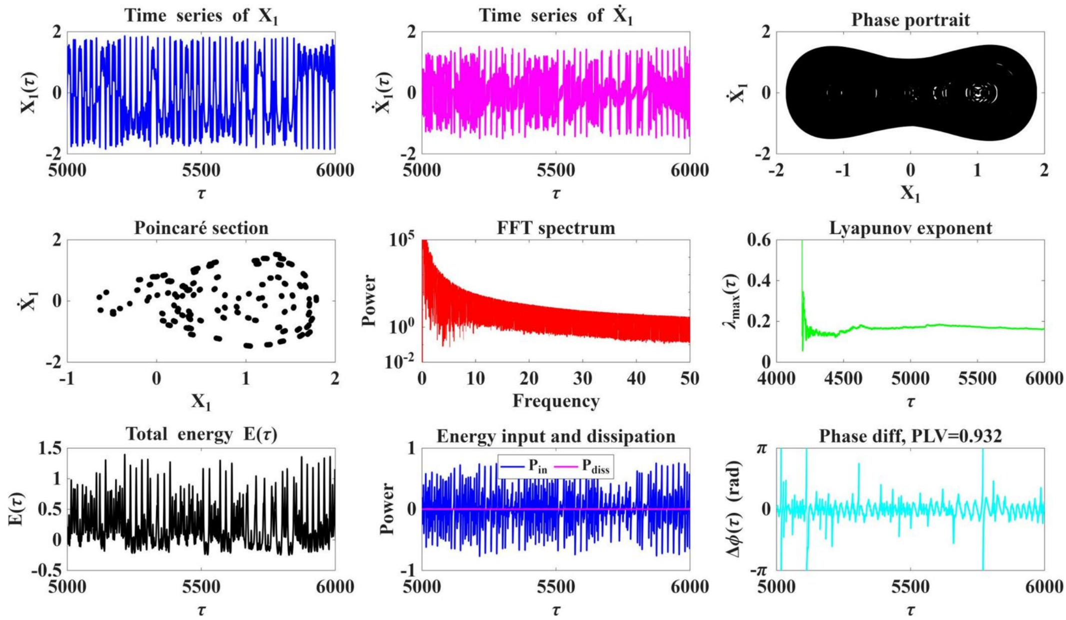

Figure 8. System response results based on parameters $s = -1, \zeta = 2 \times 10^{-3}, \eta = 0.02, \gamma = 0.01, \alpha = 1, \Omega = 0.3, F = 0.5$.

constant with a phase-locking level close to unity, reflecting strong coordination between the oscillator and eccentric block.

B. The phase portrait of the oscillator exhibited a double-loop structure, and the stroboscopic Poincaré section formed a dense crescent-shaped band rather than collapsing to a single point (or a few isolated points). The FFT spectrum showed pronounced components around the excitation frequency with broadened sidebands and an elevated spectral floor (partly attributable to finite sampling and nonlinear energy redistribution). Meanwhile, the running estimate of the largest Lyapunov exponent became slightly positive and exhibited a gradual convergence trend. Since the absolute value of the LLE may depend on numerical settings (e.g., step size, sampling, and perturbation magnitude), the present result is interpreted mainly through its sign and convergence behavior, suggesting that the system has departed from purely periodic motion and entered a transition regime with weakly chaotic or quasi-periodic features. Consistently, $E(\tau)$ exhibited slow modulation superimposed on the main oscillation, implying that the net energy balance varied over longer time scales. Correspondingly, $P_{in}(\tau)$ and $P_{diss}(\tau)$ were no longer perfectly cycle-balanced and showed intermittent mismatch, which promotes gradual energy redistribution and response modulation. The phase difference $\Delta\phi(\tau)$ displayed noticeable drift and fluctuations, and the synchronization level decreased compared with case A, indicating weakened phase locking between the two coupled components.

C. The oscillator exhibited strongly irregular and aperiodic dynamics. The displacement and velocity time histories showed pronounced amplitude modulation and random-like fluctuations, and the phase portrait became densely filled over a wide region rather than forming a simple closed curve. The Poincaré map consisted of a scattered cloud of points instead of collapsing into a finite set, indicating a loss of periodicity. The frequency spectrum displayed a broad continuous distribution with an elevated background level, which is consistent with chaotic dynamics. Meanwhile, the running estimate of the LLE stayed positive and showed a stable convergence trend after the initial transient, which supports the identification of chaotic dynamics when considered together with the other diagnostics. From the energy perspective,

$E(\tau)$ fluctuated irregularly with intermittent bursts, indicating strong non-stationary energy exchange within the coupled system. The injected and dissipated powers became highly intermittent and no longer exhibited a repeatable cycle-to-cycle balance, which is consistent with sustained non-periodic energy transfer. In addition, $\Delta\phi(\tau)$ varied erratically over a wide range and the synchronization level further decreased, reflecting a loss of coordinated motion between the oscillator and eccentric block that accompanies the chaotic regime.

By combining Figures 5–8, it can be observed that the Melnikov-predicted chaos-threshold map aligns well with the system's dynamic response. When the system resides in the periodic region, its response remains periodic; however, upon entering the non-periodic region, the response exhibits distinct chaotic behavior. The agreement supports the use of the Melnikov threshold as a first-order predictor within the investigated parameter range. For practical applications of the compaction drum model, it is recommended that the selected external excitation be kept below the chaotic threshold to ensure the system's observability and controllability.

Additionally, to highlight the significant differences between the 2-DOF and SDOF models, their dynamic responses were further compared. In the SDOF model, the oscillator and eccentric block are modeled as an integrated unit. The same parameter combinations used in Figures 6–8 were selected for comparison, with the results shown in Fig. 9. As illustrated in Fig. 9, although the two models may exhibit similar periodic responses under some low-excitation conditions, clear discrepancies arise once the coupling-induced internal dynamics become non-negligible. In particular, the phase portraits and Poincaré sections show that the 2-DOF model can display markedly different attractor structures and motion classifications compared with the lumped SDOF model, including non-periodic responses that are absent or significantly weakened in the SDOF prediction under the same (Ω, F) settings. The total energy evolution further indicates that the explicit oscillator–eccentric block coupling enables additional energy exchange pathways, which alters the response stability and the transition tendency toward complex dynamics. The comparison shows that the 2-DOF model captures coupling-induced attractor structures and non-periodic responses that are absent or substantially weakened in the SDOF model.

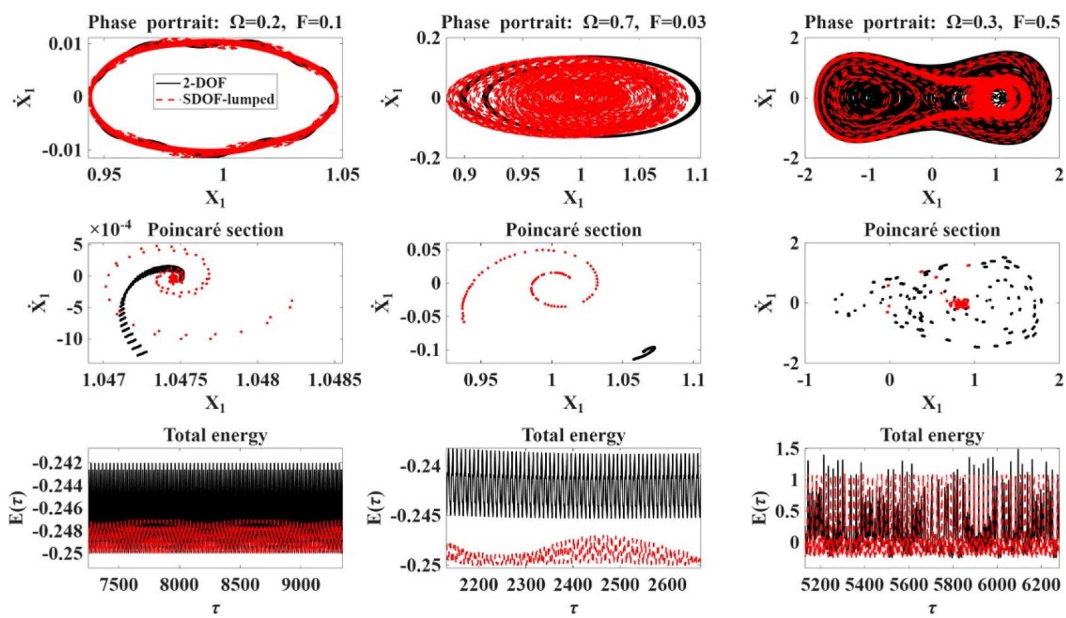

Figure 9. Dynamic response comparison between 2-DOF and SDOF models.

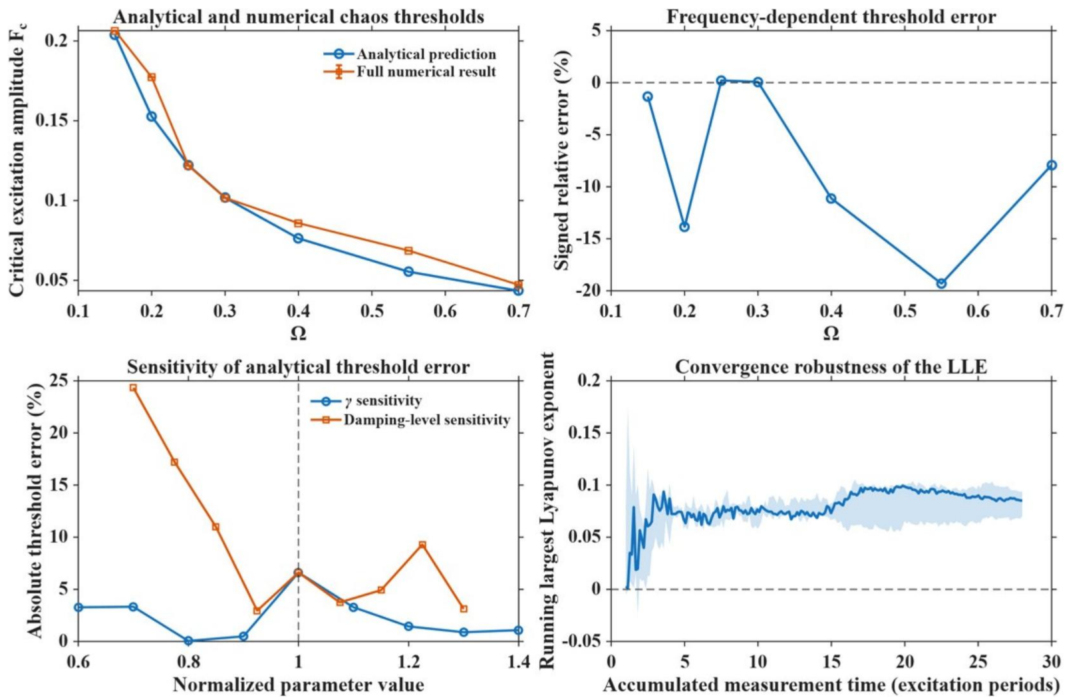

Figure 10. Quantitative validation and robustness assessment of the Melnikov chaos threshold.

In addition, Fig. 10 provides a systematic comparison between the Melnikov-based analytical threshold and the complete numerical results. The upper-left panel shows that the two threshold curves exhibit the same frequency-dependent decreasing trend and agree particularly well over the low-to-intermediate frequency range. The upper-right panel further quantifies this agreement: the signed relative error is close to zero at several frequencies, while the analytical model generally produces a conservative underestimation of the numerical threshold at higher frequencies. The largest discrepancy occurs near $\Omega = 0.55$, but the analytical prediction still correctly captures the overall variation and the location of the transition boundary. These results indicate that the reduced Melnikov formulation provides a reliable first-order estimate of chaos onset despite the small-mass-ratio, weak-damping, and decoupling approximations used in its derivation.

The lower-left panel shows that the analytical threshold is comparatively insensitive to variations in the mass ratio, with the corresponding error remaining small over most of the investigated range. By contrast, the damping-level sensitivity is more pronounced, especially when the damping is substantially below its baseline value, indicating that the weak-damping approximation is the primary source of quantitative uncertainty. Around the baseline condition, both sensitivity curves remain within a relatively limited error range, supporting the applicability of the analytical criterion to the parameter regime considered in this study. The lower-right panel confirms the numerical robustness of the largest Lyapunov exponent calculation: after the initial transient, the running exponent remains positive and converges to a stable range, while the dispersion among different integration steps and renormalization intervals gradually narrows. The consistently positive convergence envelope supports the identification of the selected response as chaotic and demonstrates that this classification is not sensitive to the numerical settings used in the Lyapunov calculation.

In summary, the Melnikov analysis provides an analytical boundary for estimating the onset of complex non-periodic motion in the coupled system. The numerical diagnostics distinguish the regular periodic, transitional weakly chaotic or quasi-periodic, and fully chaotic regimes through their attractor structures, spectra, energy-transfer behavior, phase coordination, and Lyapunov exponents. Comparison with the complete 2-DOF simulations confirms that the analytical threshold captures the principal frequency-dependent trend, although damping-related approximations introduce greater uncertainty than variations in the small mass ratio. The consistently positive and convergent Lyapunov estimates obtained under different numerical settings further support the robustness of the identified chaotic response.

5. Delayed feedback control

Furthermore, DF control was considered to increase the threshold for chaos. Based on Equation (5), critical excitation was further determined by introducing a small parameter analogous to Equation (22):

$$\begin{aligned} 2\zeta &= \varepsilon\tilde{\zeta}, \\ \eta &= \varepsilon\tilde{\eta}, \\ \kappa_c &= \varepsilon\tilde{\kappa}_c. \end{aligned} \tag{49}$$

Substituting Equation (49) into the first equation of Equation (5) yields:

$$\ddot{X}_1 + sX_1 + X_1^3 = F\cos(\Omega\tau) - \varepsilon\left[\left(\tilde{\zeta} + \tilde{\eta}\right)\dot{X}_1 - \tilde{\kappa}_c X_1(\tau - \tilde{\tau})\right]. \tag{50}$$

Performing a first-order Taylor expansion of $X_1(\tau - \tilde{\tau})$ yields:

$$X_1(\tau - \tilde{\tau}) = X_1(\tau) - \tilde{\tau}\dot{X}_1(\tau) + O(\tilde{\tau}^2). \tag{51}$$

It is noted that the first-order Taylor approximation in Equation (51) is valid under a small-delay assumption, i.e., the delay $\tilde{\tau}$ is sufficiently small compared with the dominant time scales of the system response. In nondimensional terms, this typically requires $\tilde{\tau}\Omega \ll 1$. Under this condition, the neglected higher-order terms $O(\tilde{\tau}^2)$ remain small.

Substituting Equation (51) back into Equation (50) yields:

$$\ddot{X}_1 + sX_1 + X_1^3 = F\cos(\Omega\tau) - \varepsilon\left[\left(\tilde{\zeta} + \tilde{\eta} + \tilde{\kappa}_c\tilde{\tau}\right)\dot{X}_1 - \tilde{\kappa}_c X_1\right]. \tag{52}$$

For the analytical threshold calculation, the same small-mass-ratio reduction introduced in Section 4 is retained, so that the eccentric-block coordinate is eliminated at leading order and the influence of DF control is represented in the primary-oscillator equation. This SDOF reduction is used only to obtain a tractable Melnikov criterion and does not replace the original coupled 2-DOF control model.

The remaining derivation process is analogous to Equations (57)–(65) and is not repeated here. When we again choose the most favorable case where the phase of the Melnikov function makes the cosine equal to 1 ($\cos(\Omega\tau_0) = 1$), the critical excitation is:

$$F_{critical}(\Omega) = \frac{2\sqrt{2}}{3\pi}|s|^{\frac{3}{2}}\left(\tilde{\zeta} + \tilde{\eta} + \tilde{\kappa}_c\tilde{\tau}\right)\operatorname{sech}^{-1}\left(\frac{\pi\Omega}{2\sqrt{|s|}}\right). \tag{53}$$

According to Equation (53), Fig. 11 compares the chaos thresholds under DF control for various parameter combinations. Compared with the original threshold curve, DF control significantly increased the threshold for chaos. This behavior can be interpreted from an energy-balance perspective. Using the first-order delay approximation in Equations (51) and (52), the delayed feedback term $-\tilde{\kappa}_c X_1(\tau - \tilde{\tau})$ can be decomposed into an effective stiffness contribution $-\tilde{\kappa}_c X_1$ and an additional velocity-proportional term $-\tilde{\kappa}_c\tilde{\tau}\dot{X}_1(\tau)$, which acts as an equivalent active damping. Consequently, increasing the control gain κ_c and/or the delay $\tilde{\tau}$ raises the effective dissipation level, as reflected by the factor $\left(\tilde{\zeta} + \tilde{\eta} + \tilde{\kappa}_c\tilde{\tau}\right)$ in Equation (53). Physically, stronger dissipation means that a larger external excitation amplitude is required to compensate for the increased

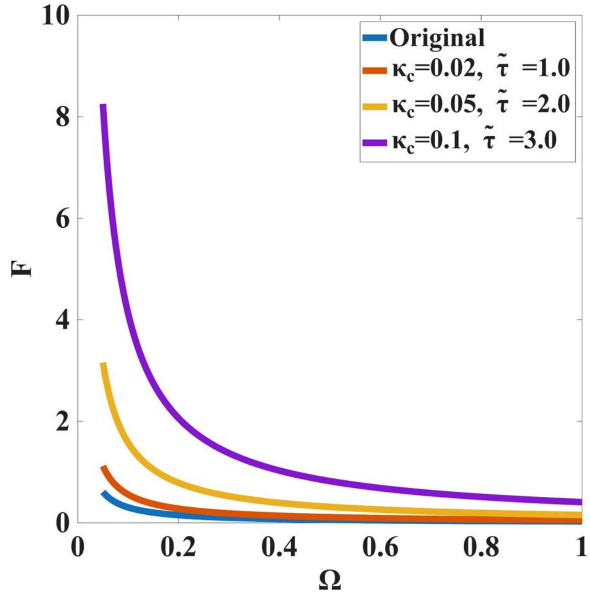

Figure 11. Comparison of different chaos thresholds for DF control based on parameters $s = -1, \zeta = 2 \times 10^{-3}$, $\eta = 0.02, \gamma = 0.01, \alpha = 1$.

energy loss per cycle before the onset of chaotic motion. Therefore, the critical excitation $F_{critical}$ increases over a wider frequency range, leading to the broadened chaotic threshold curves observed in Fig. 11.

Guided by Equation (53), the delay was confined to the small-delay regime, while the gain–delay combinations were varied systematically to examine how the effective dissipation $\tilde{\kappa}_c\tilde{\tau}$ influences the chaos threshold and the controlled response. Representative parameter sets spanning progressively stronger control levels were then selected from this parametric investigation and further verified using the complete DDE model. Similar gain–delay selection procedures based on stability characteristics and controlled-response evaluation have been employed in related delayed-feedback studies (Kumar et al. 2025; Kumar and Mitra 2023; Prasad, Mitra, and Gayen 2026).

The parameter combinations shown in Fig. 11 were employed to implement DF control for the case described in Fig. 8. In this study, the dde23 (Shampine and Thompson 2001) function in MATLAB was used to numerically solve the DDE in Equation (5). The relative and absolute error tolerances were set to 10^{-8} and 10^{-9}, respectively, and the maximum step size was restricted to $\frac{1}{2}T\Omega = \pi/\Omega$, where $T\Omega = 2\pi/\Omega$ denotes the excitation period, consistent with the stricter ode45 settings adopted for the long-time nonlinear simulations. A constant history function equal to the initial state specified in Equation (11) was prescribed over $-\tau \leq t \leq 0$, and the adaptive solution was subsequently evaluated at equally spaced time points for the phase-space, Poincaré, spectral, energy, and Lyapunov analyses. All other dde23 options retained their MATLAB default values.

The subsequent numerical assessment is performed using the complete 2-DOF DDE model, with the oscillator–eccentric-block coupling and both state coordinates fully retained. The reduced analytical threshold serves as a first-order design reference; its quantitative conclusions may become less accurate when the mass ratio, coupling strength, or delay departs from the assumed regime and should be verified using the complete model under such conditions.

The controlled responses are presented in Figures 12–14. Overall, DF control drives the system from an irregular aperiodic regime to a regular bounded regime. In the phase portraits, the uncontrolled trajectory densely fills a wide region, whereas the controlled responses form clear

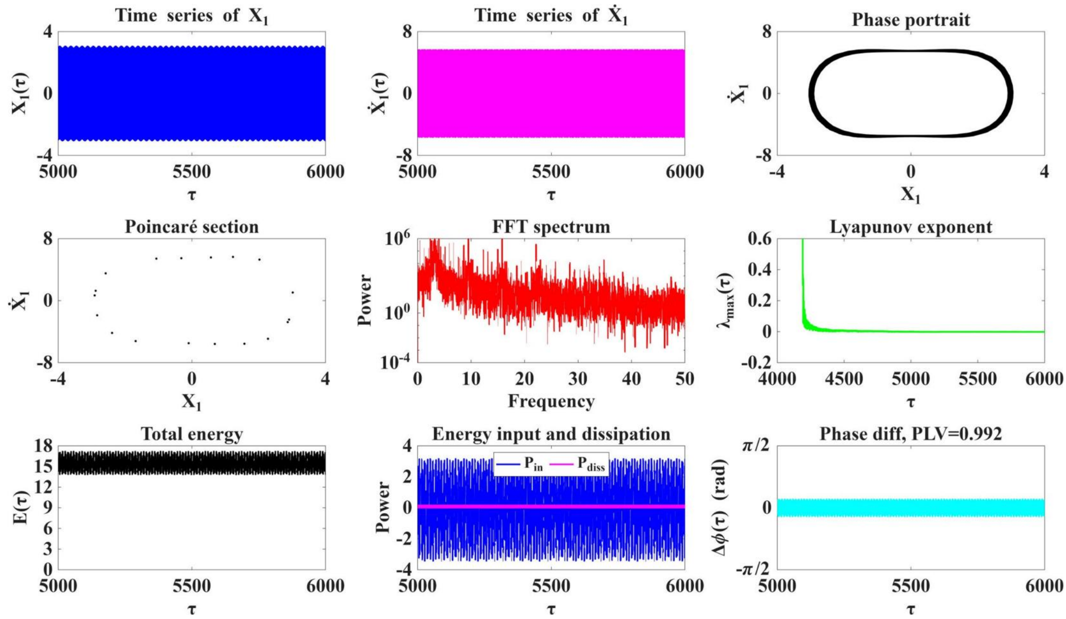

Figure 12. System response results based on parameters $s = -1, \zeta = 2 \times 10^{-3}$, $\eta = 0.02, \gamma = 0.01, \alpha = 1$, $\Omega = 0.3, F = 0.5$, $\kappa_c = 0.02, \tilde{\tau} = 1.0$.

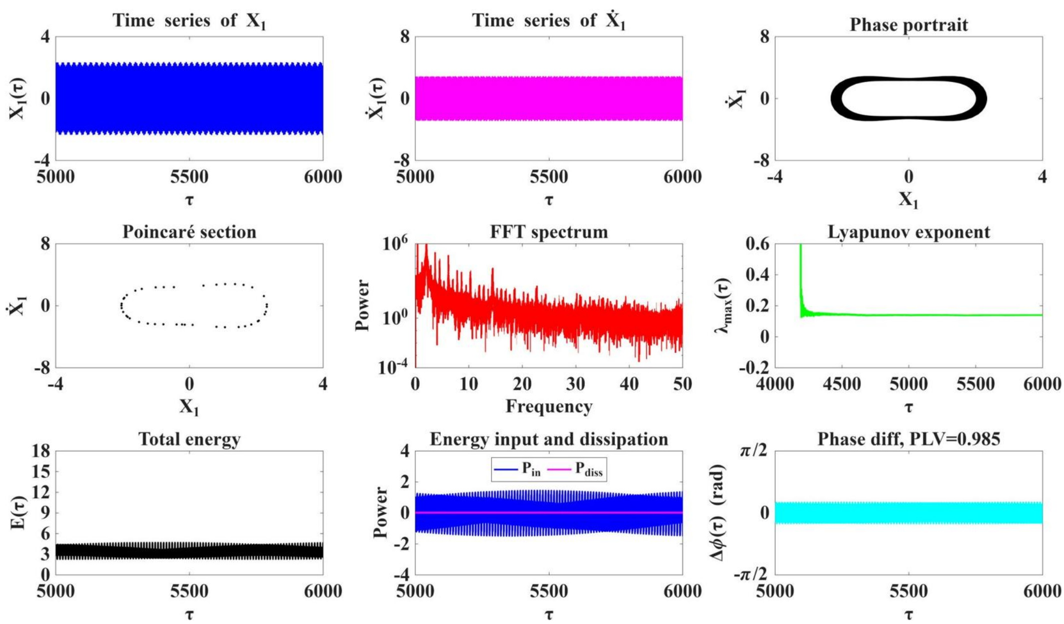

Figure 13. System response results based on parameters $s = -1, \zeta = 2 \times 10^{-3}, \eta = 0.02$, $\gamma = 0.01, \alpha = 1, \Omega = 0.3$, $F = 0.5, \kappa_c = 0.05, \tilde{\tau} = 2.0$.

closed multi-loop orbits. Consistently, the Poincaré sections change from a scattered cloud to a finite set concentrated on a closed curve, indicating the recovery of regular recurrence. As the control gain and delay increase, the oscillation amplitude of X_1 and $\dot{X}_1$ decreases and the orbit becomes more compact, demonstrating an enhanced suppression of large-amplitude motion.

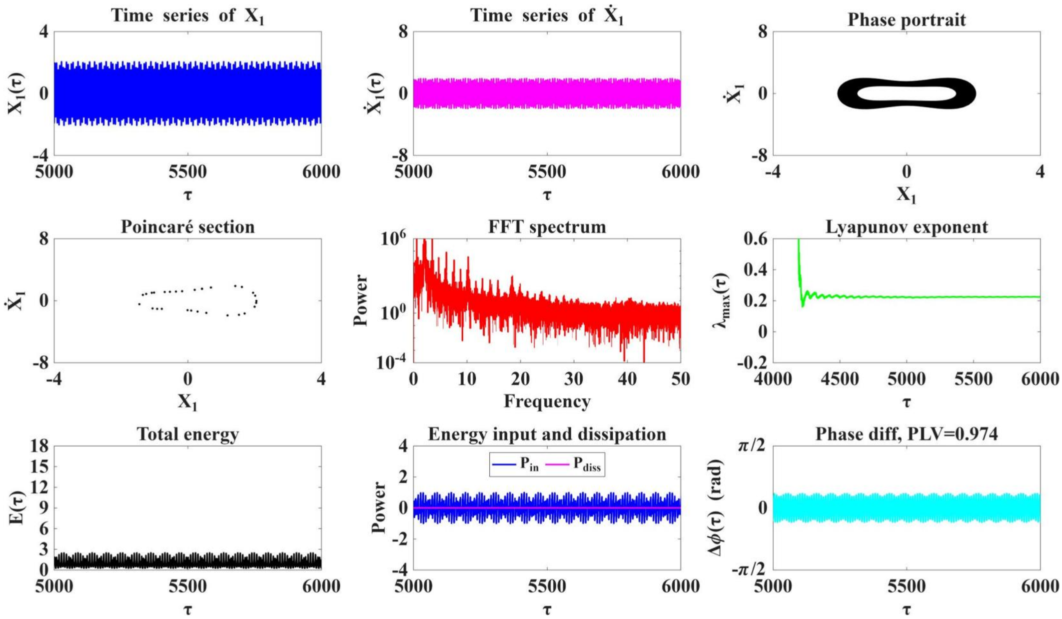

Figure 14. System response results based on parameters $s = -1, \zeta = 2 \times 10^{-3}, \eta = 0.02, \gamma = 0.01, \alpha = 1, \Omega = 0.3, F = 0.5, \kappa_c = 0.1, \tilde{\tau} = 3.0$.

After applying DF control, the total mechanical energy $E(\tau)$ becomes bounded with a more regular cycle-to-cycle pattern. Meanwhile, the injected power and the dissipated power exhibit a more consistent balance over time, indicating that DF control reduces the intermittent energy accumulation that characterizes the uncontrolled chaotic response. In addition, the phase difference between the oscillator and eccentric block becomes more constrained, and the phase-locking level remains high, showing that DF control promotes coordinated motion and suppresses desynchronization-like behavior associated with chaotic energy exchange. These observations explain physically why DF control expands the stable operating regime by regulating the net energy input and improving coupling coordination.

The running estimate of the LLE decreases markedly compared with the uncontrolled case and exhibits a stable convergence trend, which is consistent with the observed transition to regular bounded motion. The controlled system is a time-delay system with effectively infinite-dimensional dynamics, while the exponent plotted here is obtained from a finite-dimensional numerical procedure based on discretized time histories, which may yield a small positive bias in the transition regime. Therefore, the post-control dynamics are assessed by combining multiple diagnostics. The closed phase trajectories, compact Poincaré sets, regular energy evolution, and strong phase locking jointly indicate that the DF controller effectively suppresses chaos and stabilizes the response into a regular operating state, even though the finite-dimensional LLE estimate may not be strictly non-positive in all cases.

DF control was further compared with displacement-based and velocity-based feedback control. For displacement feedback control, the control force in Equation (5) becomes:

$$\tilde{F}_c = -K_p X_1(\tau), \tag{54}$$

where K_p is the displacement feedback gain.

For velocity feedback control, the control force in Equation (5) becomes:

$$\tilde{F}_c = -C_v \dot{X}_1(\tau), \tag{55}$$

where C_v is the velocity feedback gain.

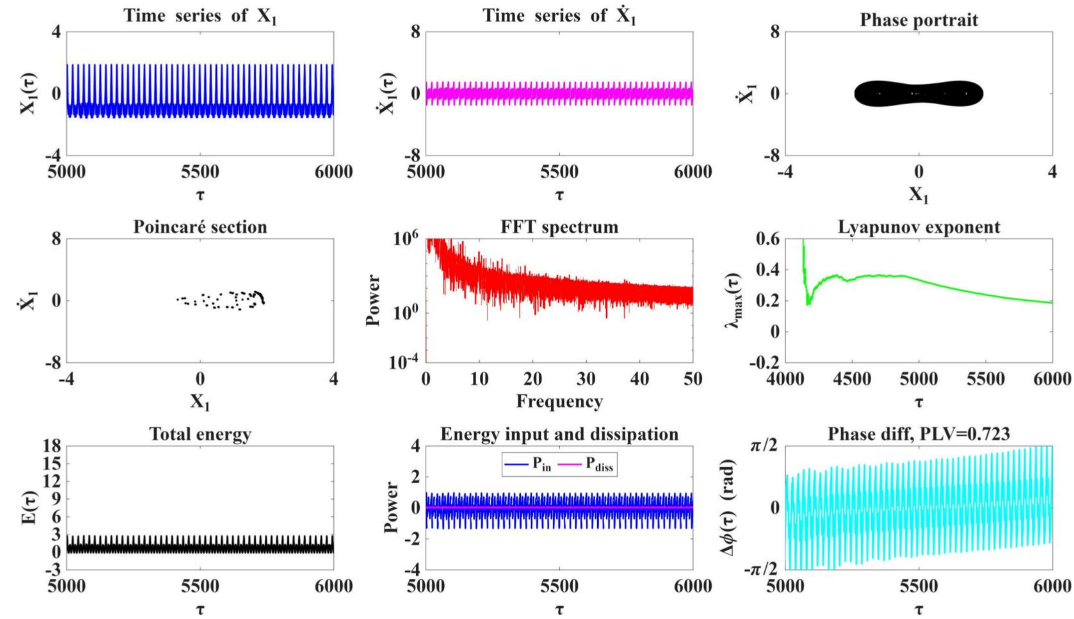

Figure 15. System response results based on displacement-based feedback control ($K_p = 0.1$).

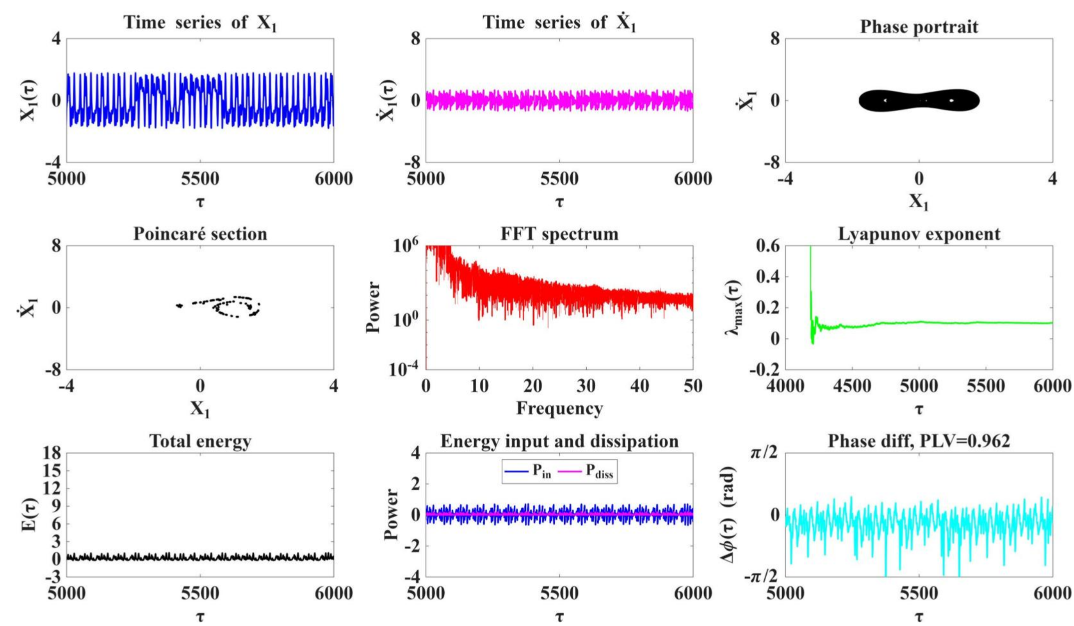

Figure 16. System response results based on velocity-based feedback control ($C_v = 0.1$).

Following the same simulation setup used in Figures 12–14, comparable gain magnitudes were adopted for the two benchmark controllers ($K_p = 0.1$, $C_v = 0.1$). The response results of the controlled system are summarized in Figures 15 and 16, respectively.

Compared with the traditional controllers, DF control yields a more pronounced regularization of the nonlinear response in the phase plane and Poincaré section. Under DF control, the phase trajectories become more organized and the Poincaré set contracts more clearly, whereas instantaneous displacement/velocity feedback still leads to a broader phase-space spread and a more scattered Poincaré distribution. Consistently, the FFT spectra indicate that DF control suppresses broadband components more effectively, while the benchmark controllers retain relatively stronger broadband content. In addition, the synchronization-related indicator provides further evidence of the coupling regulation effect. As shown by the phase-difference panel and the corresponding PLV value, DF control achieves a stronger phase-locking tendency between the oscillator and the eccentric block than the instantaneous feedback benchmarks, indicating a more coherent coupled motion. This enhanced phase coordination is also consistent with the observed reduction of irregular response features (phase-space dispersion and broadband spectral content) under DF control.

Overall, compared with instantaneous displacement/velocity feedback, DF control provides a clearer regularization of the nonlinear response, evidenced by a more compact Poincaré set and a stronger suppression of broadband spectral components. Moreover, the higher PLV under DF control indicates improved phase coherence between the oscillator and the eccentric block, highlighting the superior effectiveness of DF control in stabilizing the coupled dynamics.

In addition, Fig. 17 further evaluates the robustness of DF control by quantifying how small perturbations in the control gain κ_c and time delay $\tilde{\tau}$ affect the vibration-suppression performance. The contour maps report the normalized root mean square (RMS) index J/J_0 and normalized peak index A/A_0 of X_1, where values closer to 1 indicate performance close to the baseline controlled case and larger values indicate degraded suppression. Overall, the results show that the control effectiveness varies smoothly in the $(\kappa_c, \tilde{\tau})$ plane, without abrupt performance loss for small parameter deviations, suggesting a robust operating region.

The sensitivity slices provide more direct insight. For a fixed delay ($\tilde{\tau} = 2$), increasing κ_c leads to only a gradual change in J/J_0, indicating that moderate gain perturbations do not significantly deteriorate the RMS suppression. For a fixed gain ($\kappa_c = 0.2$), increasing $\tilde{\tau}$ causes a clear reduction in J/J_0, implying that the time-delay setting plays a more influential role in improving suppression within the tested range. Consistently, the peak-response map A/A_0 exhibits the same qualitative trend as the RMS map, confirming that the robustness conclusion holds for both average and extreme vibration measures.

In addition, although Equation (53) shows that the first-order chaos threshold increases with the effective damping contribution $k_c\tilde{\tau}$, it does not provide a finite unconstrained optimum because increasing either parameter continuously raises the predicted threshold within the small-delay approximation. In practice, k_c and $\tilde{\tau}$ may be selected through constrained numerical

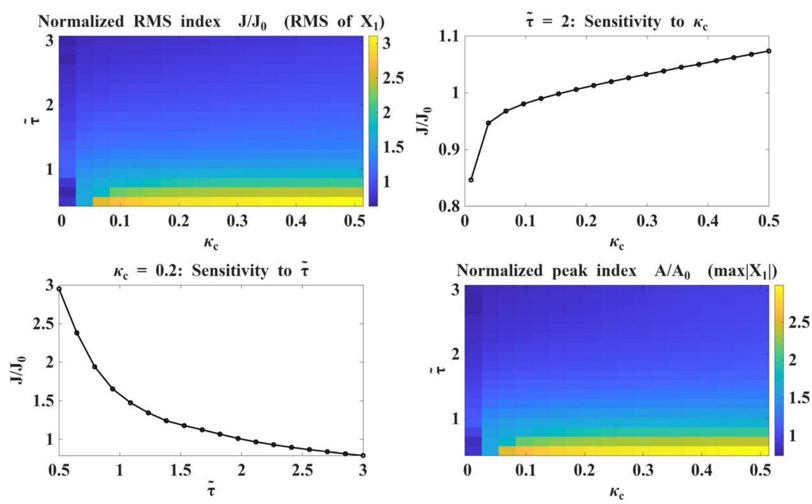

Figure 17. Influence of small perturbations in control gain κ_c and time delay $\tilde{\tau}$ on control effectiveness.

optimization by minimizing a weighted combination of the RMS or peak response and control effort while satisfying actuator, delay, and stability limits, with the parameter maps in Fig. 17 providing a feasible design domain. A limitation of DF control is that the optimal parameter combination depends on the operating condition, while excessive gain or delay may increase actuator demand, produce unfavorable phase shifts, invalidate the small-delay approximation, or even destabilize the closed-loop system.

In practical implementation, the DF controller could be realized using a displacement sensor mounted on the oscillator, a real-time digital controller that stores the measured response over the prescribed delay interval, and an electromechanical or hydraulic actuator that applies the resulting control force (Feng 2025a, 2026c). Such a prescribed delay can be implemented in a digital feedback loop by sampling the sensor signal, storing it in a finite memory buffer, and retrieving the corresponding past value at each control step, as demonstrated by digital signal processor-based DF experiments on flexible structures and digital vibration-control studies of suspended cables (Cai and Chen 2010; Kollár 2021). The smooth response variations observed in Fig. 17 indicate that moderate errors in the control gain and delay do not cause an abrupt loss of effectiveness, although the delay should be tuned with particular care because it directly determines the phase relationship between the control action and the drum motion. Compared with instantaneous displacement or velocity feedback, DF control provides an additional phase-adjustment capability and does not require an externally prescribed reference trajectory; however, its implementation requires signal storage and accurate timing, and its performance may be affected by sensor noise, actuator saturation, computational latency, time-varying operating conditions, and uncertainty in the drum parameters. Moreover, because the present model does not include drum–ground interaction, experimental calibration and hardware-in-the-loop or field validation is required before the proposed controller can be directly applied to practical compaction machinery.

In summary, DF control raises the predicted chaos threshold and transforms the uncontrolled irregular response into a more regular and bounded motion by increasing effective dissipation and regulating the phase relationship between the coupled components. Compared with instantaneous displacement and velocity feedback, DF control produces more compact attractors, weaker broadband spectral content, and stronger phase coordination. The control effectiveness also varies smoothly under moderate perturbations of the gain and delay, indicating a useful degree of parameter robustness, although accurate delay tuning remains important.

6. Discussion

Building on the above analytical and numerical results, this section discusses the practical implications of the proposed framework and summarizes its main advantages in two aspects, namely dynamic response prediction accuracy and chaos control efficiency. A key advantage of the present framework is that the internal exciter dynamics are represented explicitly through the two-mass coupling, which naturally separates a global drum-dominated motion from a relative-motion component associated with the eccentric block. This modal separation provides an interpretable mechanism for response changes across operating conditions and helps explain why a lumped SDOF description may miss or misclassify complex responses. In particular, once the relative motion becomes non-negligible, the coupled system admits additional energy-transfer pathways between the two components, so that qualitatively different long-term behaviors can arise under the same external excitation. From the perspective of response prediction, the 2-DOF formulation therefore improves the model's ability to discriminate between periodic, transitional, and fully non-periodic regimes in a physically meaningful way, rather than attributing all response changes to a single effective coordinate.

Compared with instantaneous feedback strategies, delayed feedback provides an additional degree of freedom in shaping the phase relationship between the control action and the system motion. This feature is particularly beneficial in coupled nonlinear dynamics, where suppressing irregular responses requires not only reducing amplitudes but also regulating coordination between subsystems. In the present model, DF control improves the coherence of the coupled motion by promoting phase coordination between the oscillator and the eccentric block, which in turn reduces irregular energy exchange and mitigates intermittent energy accumulation. As a result, the controlled responses exhibit a clearer tendency toward regular bounded motion over a wider parameter neighborhood, indicating that DF control can achieve stabilization without relying solely on high instantaneous gains. From an engineering standpoint, this phase-aware regulation mechanism provides a practical explanation for the observed expansion of stable operation and the improved robustness of the control effect with respect to small parameter perturbations. In practical compaction operations, however, system parameters may vary due to manufacturing tolerances, material property changes, structural wear, and varying working conditions. Therefore, a meaningful direction for future research is to extend the present framework to include parameter disturbances and time-varying uncertainties, so that the dynamic prediction and controller parameter design can better reflect the complexity of real operating environments.

7. Conclusion

This study developed a nonlinear 2-DOF model of a compaction drum that explicitly represents the internal coupling between the oscillator and the eccentric block and incorporates DF control. The harmonic balance and numerical results revealed pronounced nonlinear resonance and jump behavior, while the comparison with Den Hartog's estimates showed that the near-optimal stiffness is relatively robust but the damping optimum is more sensitive to nonlinear resonance distortion. The Melnikov analysis provided a first-order analytical criterion for chaos onset, and its predictive capability was assessed against the complete numerical model using threshold errors, sensitivity analysis, phase portraits, Poincaré sections, FFT spectra, and Lyapunov-exponent robustness tests. The results demonstrate that internal coupling creates energy-transfer pathways and dynamical transitions that cannot be represented adequately by a lumped SDOF model.

The DF controller increased the chaos threshold and transformed irregular responses into more regular and bounded motions by modifying the effective dissipation and phase relationship between the coupled components. The accompanying energy, power-balance, and phase-locking analyses indicate that the controller suppresses intermittent energy accumulation and promotes coordinated oscillator–eccentric-block motion. More broadly, the proposed framework connects analytical chaos prediction, complete nonlinear simulation, and active control within a unified model, providing a useful basis for identifying unstable operating regions and selecting excitation and control parameters in vibratory machinery. Nevertheless, the conclusions are limited by the planar lumped-parameter representation, the omission of drum–ground interaction and vertical compaction dynamics, the small-mass-ratio, weak-damping, and small-delay assumptions used in the analytical reductions, and the absence of experimental validation. Accordingly, the present engineering implications should be interpreted as theoretically informed guidance rather than direct field-performance predictions.

Future work should first identify model and control parameters from instrumented drum measurements and validate the predicted thresholds and control effects through laboratory, hardware-in-the-loop, and field experiments. The model can then be extended to higher-dimensional systems that include the drum, frame, cab, soil or asphalt layer, contact loss, material nonlinearity, and spatially varying support conditions. More complex delay formulations should also be investigated, including multiple and time-varying delays, distributed delays, and neutral-delay systems containing delayed velocity or acceleration terms, for which stability, bifurcation, and chaos-control conditions may differ substantially from those derived here. Adaptive or robust controllers that account for sensor noise, actuator saturation, parameter uncertainty, and changing operating conditions would further support the development of reliable intelligent compaction systems.

Acknowledgments

The author also thanks five anonymous reviewers and the editor for their valuable comments on earlier versions of this article.

Author contributions

CRediT: **Dong Feng**: Conceptualization, Data curation, Formal analysis, Funding acquisition, Investigation, Methodology, Project administration, Resources, Software, Validation, Visualization, Writing – original draft, Writing – review & editing.

Disclosure statement

No potential conflict of interest was reported by the authors.

Funding

This work was supported by the China Scholarship Council under Grant 202308080042.

References

Abdelmonem, Hany Samih Bauomy. 2025. "Dual Nonlinear Saturation Control of Electromagnetic Suspension (EMS) System in Maglev Trains." *Mathematics* 14 (1): 62. https://doi.org/10.3390/math14010062

Anderegg, R., and K. Kaufmann. 2004. Intelligent Compaction with Vibratory Rollers: Feedback Control Systems in Automatic Compaction and Compaction Control. *Transportation Research Record*. https://www.semanticscholar.org/paper/Intelligent-Compaction-with-Vibratory-Rollers%3A-in-Anderegg-Kaufmann/c21ce77b667fcaa5231026e6164039e5b8e195d0

Batey, T. 2009. "Soil Compaction and Soil Management – A Review." *Soil Use and Management* 25 (4): 335–345. https://doi.org/10.1111/j.1475-2743.2009.00236.x

Bauomy, Hany Samih. 2024. "Advanced Vibrant Controller Results of an Energetic Framework Structure." *Open Engineering* 14 (1): 20240055. https://doi.org/10.1515/eng-2024-0055

Bauomy, Hany Samih. 2025. "Active Control Impact Analysis on Shaped Coupled Beam Structure." *AIMS Mathematics* 10 (12): 30732–30772. https://doi.org/10.3934/math.20251349

Bauomy, Hany Samih, and Ashraf Taha EL-Sayed. 2025. "Oscillation Controlling in Nonlinear Motorcycle Scheme with Bifurcation Study." *Mathematics* 13 (19): 3120. https://doi.org/10.3390/math13193120

Beainy, Fares, Sesh Commuri, and Musharraf Zaman. 2014. "Dynamical Response of Vibratory Rollers during the Compaction of Asphalt Pavements." *Journal of Engineering Mechanics* 140 (7): 04014039. https://doi.org/10.1061/(ASCE)EM.1943-7889.0000730

Blondel, A. 1919. "Amplitude du Courant Oscillant Produit Par Les Audions Générateurs: Comptes Rendus Hebdomadaires Des Séances de L'Académie Des Sciences 169.17."

Cai, Guo-Ping, and Long-Xiang Chen. 2010. "Delayed Feedback Control Experiments on Some Flexible Structures." *Acta Mechanica Sinica* 26 (6): 951–965. https://doi.org/10.1007/s10409-010-0388-6

Chen, Aijun, Feng Cheng, Di Wu, and Xianyuan Tang. 2019. "Ground Vibration Propagation and Attenuation of Vibrating Compaction." *Journal of Vibroengineering* 21 (5): 1342–1352. https://doi.org/10.21595/jve.2019.20388

Chen, Yueli, Kwok-wai Chung, Jian Xu, and Yixia Sun. 2014. "Analysis of Vibration Suppression of Master Structure in Nonlinear Systems Using Nonlinear Delayed Absorber." *International Journal of Dynamics and Control* 2 (1): 55–67. https://doi.org/10.1007/s40435-014-0081-x

Cui, Xinzhuang, Shirong Yan, Xiaoning Zhang, Junhao Zhou, Qing Jin, and Yefeng Du. 2024. "Research on the Coupled Dynamic Response of Vibratory Roller-Unsaturated Subgrade under Different Compaction and Moisture Content States." *Transportation Geotechnics* 46: 101252. https://doi.org/10.1016/j.trgeo.2024.101252

Dormand, J. R., and P. J. Prince. 1980. "A Family of Embedded Runge-Kutta Formulae." *Journal of Computational and Applied Mathematics* 6 (1): 19–26. https://doi.org/10.1016/0771-050X(80)90013-3

Du, Shaowen. 2025. "Effect of Secondary Compaction on the Performance Properties of Asphalt Emulsion-Recycled Mixture with Atmospheric Temperature Curing." *Journal of Materials in Civil Engineering* 37 (10): 04025338. https://doi.org/10.1061/JMCEE7.MTENG-20658

Fan, Liming, Chen Huang, and Linsheng Huo. 2024. "Equivalent Linearization and Parameter Optimization of the Negative Stiffness Bistable Damper." *Buildings* 14 (3): 744. https://doi.org/10.3390/buildings14030744

Fang, Xiaojun, Yongming Bian, Meng Yang, and Guangjun Liu. 2018. "Development of a Path following Control Model for an Unmanned Vibratory Roller in Vibration Compaction." *Advances in Mechanical Engineering* 10 (5): 1687814018773660. https://doi.org/10.1177/1687814018773660

Fang, Zhou, Yu Zhu, Tao Ma, Yang Zhang, Tao Han, and Jinglin Zhang. 2022. "Dynamical Response to Vibration Roller Compaction and Its Application in Intelligent Compaction." *Automation in Construction* 142: 104473. https://doi.org/10.1016/j.autcon.2022.104473

Feng, Dong. 2025a. "A Compactor-Soil Coupling Model considering Mechanical Inertia and Its Delayed Feedback Active Suspension Control." *International Journal of Non-Linear Mechanics* 179: 105245. https://doi.org/10.1016/j.ijnonlinmec.2025.105245

Feng, Dong. 2025b. "Multi-Scale Algorithm for Controllable Virtual Aggregate Generation in Mesoscale Modeling." *International Journal of Mechanical Sciences* 308: 110978. https://doi.org/10.1016/j.ijmecsci.2025.110978

Feng, Dong. 2026a. "A DEM-Based Particle–Force Chain Informatics Framework for Data-Driven Evaluation of Pavement Pre-Compaction." *Advanced Engineering Informatics* 71: 104402. https://doi.org/10.1016/j.aei.2026.104402

Feng, Dong. 2026b. "A Fully Coupled FBSDE Framework for Optimal Orbit Steering near an Arneodo-Coullet-Tresser Spiral Attractor." *Communications in Nonlinear Science and Numerical Simulation* 162: 110319. https://doi.org/10.1016/j.cnsns.2026.110319

Feng, Dong. 2026c. "A Novel Four-Degree-of-Freedom Compactor–Soil Coupling Model." *Nonlinear Dynamics* 114 (8). https://doi.org/10.1007/s11071-026-12419-6

Feng, Dong. 2026d. "A Quadratic BSDE Framework for Risk-Adjusted Noise-Induced Switching in Bistable Nonlinear Oscillators under Stochastic Volatility." *Chaos, Solitons & Fractals* 207: 118021. https://doi.org/10.1016/j.chaos.2026.118021

Feng, Dong. 2026e. "Contact Selection Chaos of Two Analytical Gömböcs under Biharmonic Vertical Excitation." *Chaos, Solitons & Fractals* 209: 118539. https://doi.org/10.1016/j.chaos.2026.118539

Feng, Dong. 2026f. "Spectral Contact Networks for Granular Base Load Spreading." *International Journal of Mechanical Sciences* 326: 111914. https://doi.org/10.1016/j.ijmecsci.2026.111914

Feng, Dong, Chaoliang Fu, and Pengfei Liu. 2026. "A Modified Johnson-Kendall-Roberts Contact Model for Pavement Engineering: Consideration of Time-Dependent Surface Energy." *Powder Technology* 468: 121701. https://doi.org/10.1016/j.powtec.2025.121701

Feng, Dong, Chaoliang Fu, Kai Zheng, Tianling Wang, and Chonghui Wang. 2026. "Numerical Framework for Asphalt Pre-Compaction Optimization Using a Coarse-Graining Discrete Element Method (DEM)." *Powder Technology* 478: 122486. https://doi.org/10.1016/j.powtec.2026.122486

Feng, Dong, Jinchao Guan, Chaoliang Fu, Yuanyuan Hu, Frederic Otto, Alvaro García Hernandez, and Pengfei Liu. 2026. "Augmentation of 3D Virtual Aggregate Database Using Deep Convolutional Wasserstein Generative Adversarial Networks." *Advanced Engineering Informatics* 69: 103994. https://doi.org/10.1016/j.aei.2025.103994

Feng, Dong, and Kai Zheng. 2026. "Strongly Nonlinear Pulse Attenuation in Microgranular Chains with Fractional Contact Dissipation." *Particuology* 116: 202–213. https://doi.org/10.1016/j.partic.2026.06.009

Ginoux, J. 2017. *History of Nonlinear Oscillations Theory in France (1880–1940)*. Cham: Springer. https://link.springer.com/content/pdf/10.1007/978-3-319-55239-2.pdf

Guo, Feng, and Hui Fang. 2024. "Chaos Identification and Parameter Optimization for Vibration Suppression in Composite Bistable Structures." *Mechanics Research Communications* 135: 104236. https://doi.org/10.1016/j.mechrescom.2023.104236

Guo, Yong, Yuh-Chung Hu, and Chuan-Bo Ren. 2022. "An Optimization Algorithm of Time-Delayed Feedback Control Parameters for Quarter Vehicle Semiactive Suspension System." *Mathematical Problems in Engineering* 2022 (1): 1–9. https://doi.org/10.1155/2022/2946091

Hartog, J. P. den. 2013. Mechanical Vibrations: Dover Publications (Dover Civil and Mechanical Engineering). https://books.google.de/books?id=mtDCAgAAQBAJ Accessed on August 7, 2026

Hicken, Jason, and Vignesh Ramakrishnan. 2024. "A Method to Regularize Optimization Problems Governed by Chaotic Dynamical Systems." *Chaos, Solitons & Fractals* 188: 115491. https://doi.org/10.1016/j.chaos.2024.115491

Huang, Yedong, Dazhong Yu, Baijin Mao, Fangming Li, and Juntian Qu. 2026. "Bioinspired Morphology-Decoupled Soft Gripper with Enhanced Bidirectional Grasping Capability." *Advanced Science (Weinheim, Baden-Wurttemberg, Germany)* 13 (34): e75073 10.1002/advs.75073 . PMC: 41926677

Kollár, László E. 2021. "Digital Control of Cable Vibration with Time Delay." *International Journal of Dynamics and Control* 9 (3): 1223–1235. https://doi.org/10.1007/s40435-020-00711-1
Koruk, Hasan, and Srinath Rajagopal. 2024. "A Comprehensive Review on Viscoelastic Parameters Used for Engineering Materials Including Soft Materials and the Relationships between Different Damping Parameters." *Sensors* 24 (18): 6137. https://doi.org/10.3390/s24186137 https://doi.org/10.20944/preprints202408.0973.v1
Kumar, Ranjan, and Ranjan Kumar Mitra. 2023. "Controlling Period-Doubling Route to Chaos Phenomena of Roll Oscillations of a Biased Ship in Regular Sea Waves." *Nonlinear Dynamics* 111 (15): 13889–13918. https://doi.org/10.1007/s11071-023-08605-5
Kumar, Ranjan, Ponnada Durga Prasad, Ranjan Kumar Mitra, and Debabrata Gayen. 2025. "Delayed Feedback Control of Pitch Oscillations of an ALP Tower." *International Journal of Mechanical Sciences* 302: 110578. https://doi.org/10.1016/j.ijmecsci.2025.110578
Kumar Das, Jayanta, and Binu Sharma. 2026. "Influence of Compaction Methods on Strength, Microstructure, and Suction Characteristics of Fine-Grained Soils." *Geomechanics and Geoengineering* 21 (1): 1–19. https://doi.org/10.1080/17486025.2025.2552835
Le, Thanh Danh, and Kyoung Kwan Ahn. 2011. "A Vibration Isolation System in Low Frequency Excitation Region Using Negative Stiffness Structure for Vehicle Seat." *Journal of Sound and Vibration* 330 (26): 6311–6335. https://doi.org/10.1016/j.jsv.2011.07.039
Liu, Donghai, Youle Wang, Junjie Chen, and Yalin Zhang. 2019. "Intelligent Compaction Practice and Development: A Bibliometric Analysis." *Engineering, Construction and Architectural Management* 27 (5): 1213–1232. https://doi.org/10.1108/ECAM-05-2019-0252
Liu, Lun, Fenghui Wang, Shupeng Sun, Weiming Feng, and Chao Guo. 2021. "Nonlinear Dynamics of the Rigid Drum for Vibratory Roller on Elastic Subgrades." *Shock and Vibration* 2021 (1): 9589230–9589230. https://doi.org/10.1155/2021/9589230
Lu, Yongjie, Jingxu Liu, Junning Zhang, and Jianxi Wang. 2023. "Research on Vibratory & Oscillatory Coexistence Nonlinear Dynamics Based on Drum-Subgrade Coupling Model." *International Journal of Non-Linear Mechanics* 157: 104536. https://doi.org/10.1016/j.ijnonlinmec.2023.104536
Lu, Ze-Qi, Li-Qun Chen, Michael J. Brennan, Jue-Ming Li, and Hu Ding. 2016. "The Characteristics of Vibration Isolation System with Damping and Stiffness Geometrically Nonlinear." *Journal of Physics: Conference Series* 744 (1): 012115. https://doi.org/10.1088/1742-6596/744/1/012115
Melnikov, V. K. 1963. On the Stability of the Center for Time Periodic Perturbations: Trudy Moskovskogo Matematicheskogo Obshchestva (12). https://scispace.com/papers/on-the-stability-of-the-center-for-time-periodic-xidyc2cj3r?citations_page=134
Paulmichl, Ivan, Christoph Adam, and Dietmar Adam. 2019. "Analytical Modeling of the Stick-Slip Motion of an Oscillation Drum." *Acta Mechanica* 230 (9): 3103–3126. https://doi.org/10.1007/s00707-019-02454-3
Peng, Hu, Chen Jiazhen, Zhang Lejin, Wang Kun, Wang Shuping, and Chi Lianyang. 2024. "Discrete Element Simulation of Vibration Compaction of Slag Subgrade." *Scientific Reports* 14 (1): 5039. https://doi.org/10.1038/s41598-024-55276-2
Phohomsiri, Phailaung, Firdaus E. Udwadia, and Hubertus F. von Bremen. 2006. "Time-Delayed Positive Velocity Feedback Control Design for Active Control of Structures." *Journal of Engineering Mechanics* 132 (6): 690–703. https://doi.org/10.1061/(ASCE)0733-9399(2006)132:6(690)
Pietzsch, Dieter, and Wolfgang Poppy. 1992. "Simulation of Soil Compaction with Vibratory Rollers." *Journal of Terramechanics* 29 (6): 585–597. https://doi.org/10.1016/0022-4898(92)90038-L
Pistrol, Johannes, Mario Hager, Fritz Kopf, and Dietmar Adam. 2023. "Consideration of the Variable Contact Geometry in Vibratory Roller Compaction." *Infrastructures* 8 (7): 110. https://doi.org/10.3390/infrastructures8070110
Pistrol, Johannes, Fritz Kopf, Dietmar Adam, and Clemens Kummerer. 2024. "Deep Vibrocompaction at the Natural Frequency of the Soil Response." *Journal of Geotechnical and Geoenvironmental Engineering* 150 (9): 04024076. https://doi.org/10.1061/JGGEFK.GTENG-12351
Platus, David L. 1992. "Negative-Stiffness-Mechanism Vibration Isolation Systems." In *Vibration Control in Microelectronics, Optics, and Metrology*, edited by Colin G. Gordon, 44–54. San Jose - DL tentative. San Jose, CA, Friday 1 November 1991: SPIE (SPIE Proceedings).
Prasad, Ponnada Durga, Ranjan Kumar Mitra, and Debabrata Gayen. 2026. "Non-Smooth Bifurcation Structures and Chaos Control in a Quarter-Car Piecewise-Linear Suspension System with Time-Delayed Velocity Feedback." *International Journal of Non-Linear Mechanics* 187: 105370. https://doi.org/10.1016/j.ijnonlinmec.2026.105370
Pyragas, K. 1992. "Continuous Control of Chaos by Self-Controlling Feedback." *Physics Letters A* 170 (6): 421–428. https://doi.org/10.1016/0375-9601(92)90745-8
Pyragas, K. 1993. "Predictable Chaos in Slightly Perturbed Unpredictable Chaotic Systems." *Physics Letters A* 181 (3): 203–210. https://doi.org/10.1016/0375-9601(93)90640-L

Rainer Massarsch, K., and Bengt H. Fellenius. 2005. "Chapter 19 Deep Vibratory Compaction of Granular Soils." In *Elsevier Geo-Engineering Book Series: Ground Improvement—Case Histories*, edited by Buddhima Indraratna and Jian Chu, 539–561. Vol. 3. Amsterdam, Netherlands: Elsevier. https://www.sciencedirect.com/science/article/pii/S1571996005800229

Shampine, L. F., and S. Thompson. 2001. "Solving DDEs in Matlab." *Applied Numerical Mathematics* 37 (4): 441–458. https://doi.org/10.1016/S0168-9274(00)00055-6

Shampine, Lawrence F., and Mark W. Reichelt. 1997. "The MATLAB ODE Suite." *SIAM Journal on Scientific Computing* 18 (1): 1–22. https://doi.org/10.1137/S1064827594276424

Steffanoni, Alessandro, Michel Di Tommaso, Vito Giovanni Gallo, Giuseppe Macaluso, Carmine Rizzato, Misagh Ketabdari, and Emanuele Toraldo. 2024. "Modeling and Laboratory Investigation of Tack Coats as Bituminous Pavement Interlayer." *Buildings* 14 (8): 2358. https://doi.org/10.3390/buildings14082358

Wang, Yong, Hao-Xuan Li, Chun Cheng, Hu Ding, and Li-Qun Chen. 2021. "A Nonlinear Stiffness and Nonlinear Inertial Vibration Isolator." *Journal of Vibration and Control* 27 (11–12): 1336–1352. https://doi.org/10.1177/1077546320940924

Watanabe, Masahisa, and Awadhesh Prasad. 2025. "Fractional Delayed Feedback for Semi-Active Suspension Control of Nonlinear Jumping Quarter Car Model." *Chaos, Solitons & Fractals* 199: 116973. https://doi.org/10.1016/j.chaos.2025.116973

Watanabe, Masahisa, Awadhesh Prasad, and Kenshi Sakai. 2024. "Delayed Feedback Active Suspension Control for Chaos in Quarter Car Model with Jumping Nonlinearity." *Chaos, Solitons & Fractals* 186: 115236. https://doi.org/10.1016/j.chaos.2024.115236

Werndl, Charlotte. 2009. "What Are the New Implications of Chaos for Unpredictability?" *The British Journal for the Philosophy of Science* 60 (1): 195–220. https://doi.org/10.1093/bjps/axn053

Wersäll, C., I. Nordfelt, and S. Larsson. 2017. "Soil Compaction by Vibratory Roller with Variable Frequency." *Géotechnique* 67 (3): 272–278. https://doi.org/10.1680/jgeot.16.P.051

Wu, Longliang, Jun Teng, Zhenyang Ren, Huihuang Jiang, and Mingxian Gao. 2022. "Research on Identification Model of Continuous Compaction Based on Energy Dissipation." *Shock and Vibration* 2022: 1–13. https://doi.org/10.1155/2022/9998387

Xu, Tianyu, Zhijun Zhou, Ruipeng Yan, Zhipeng Zhang, Linxuan Zhu, Chaoran Chen, Fu Xu, et al. 2020. "Real-Time Monitoring Method for Layered Compaction Quality of Loess Subgrade Based on Hydraulic Compactor Reinforcement." *Sensors (Basel, Switzerland)* 20 (15): 4288. https://doi.org/10.3390/s20154288

Xu, Zhengheng, Hadi Khabbaz, Behzad Fatahi, and Di Wu. 2022. "Real-Time Determination of Sandy Soil Stiffness during Vibratory Compaction Incorporating Machine Learning Method for Intelligent Compaction." *Journal of Rock Mechanics and Geotechnical Engineering* 14 (5): 1609–1625. https://doi.org/10.1016/j.jrmge.2022.07.004

Yoo, Tai-Sung, and Ernest T. Selig. 1979. "Dynamics of Vibratory-Roller Compaction." *Journal of the Geotechnical Engineering Division* 105 (10): 1211–1231. https://doi.org/10.1061/AJGEB6.0000867

Yu, Kangfan, Yunwei Chen, Chuanyun Yu, Jianrun Zhang, and Xi Lu. 2024. "A Compact Nonlinear Stiffness-Modulated Structure for Low-Frequency Vibration Isolation under Heavy Loads." *Nonlinear Dynamics* 112 (8): 5863–5893. https://doi.org/10.1007/s11071-024-09334-z

Zhang, Qinglong, Zaizhan An, Zehua Huangfu, and Qingbin Li. 2022. "A Review on Roller Compaction Quality Control and Assurance Methods for Earthwork in Five Application Scenarios." *Materials (Basel, Switzerland)* 15 (7): 2610. https://doi.org/10.3390/ma15072610

Zhang, Peng, Dong Hou, Minghong Li, Quan Zhou, Guangkun Guo, Fuyu Sun, and Ke Liu. 2026. "Highly-Reliable Underwater Synchronization Based on Optical Two-Way Time Transfer at Sub-Nanosecond-Level." *Optics & Laser Technology* 203: 115624 10.1016/j.optlastec.2026.115624 .

Zhang, Yupeng, and Alan Needleman. 2020. "Influence of Assumed Strain Hardening Relation on Plastic Stress-Strain Response Identification From Conical Indentation." *Journal of Engineering Materials and Technology* 142 (3): 031002. https://doi.org/10.1115/1.4045852

Zhang, Yupeng, and Alan Needleman. 2021a. "Characterization of Plastically Compressible Solids via Spherical Indentation." *Journal of the Mechanics and Physics of Solids* 148: 104283. https://doi.org/10.1016/j.jmps.2020.104283

Zhang, Yupeng, and Alan Needleman. 2021b. "On the Identification of Power-Law Creep Parameters from Conical Indentation." *Proceedings. Mathematical, Physical, and Engineering Sciences* 477 (2252): 20210233. https://doi.org/10.1098/rspa.2021.0233

Zhao, Yan-Ying, and Jian Xu. 2007. "Effects of Delayed Feedback Control on Nonlinear Vibration Absorber System." *Journal of Sound and Vibration* 308 (1–2): 212–230. https://doi.org/10.1016/j.jsv.2007.07.041

Zhou, Chunyu, Guangdong Sui, Yifeng Chen, and Xiaobiao Shan. 2024. "A Nonlinear Low Frequency Quasi Zero Stiffness Vibration Isolator Using Double-Arc Flexible Beams." *International Journal of Mechanical Sciences* 276: 109378. https://doi.org/10.1016/j.ijmecsci.2024.109378

Zhu, Qingbo, and Kai Chai. 2024. "Magnetic Negative Stiffness Devices for Vibration Isolation Systems: A State-of-the-Art Review from Theoretical Models to Engineering Applications." *Applied Sciences* 14 (11): 4698. https://doi.org/10.3390/app14114698

Appendix A: Melnikov chaos analysis

To facilitate the use of the Melnikov method, Equation (47) was written in standard form as follows:

$$\ddot{X}_1 + \frac{\mathrm{d}V}{\mathrm{d}X_1} = \varepsilon g\left(X_1, \dot{X}_1, \tau\right), \tag{56}$$

where the potential energy is $V(X_1) = \frac{s}{2}X_1^2 + \frac{1}{4}X_1^4$, and the small perturbation is $g\left(X_1, \dot{X}_1, \tau\right) = -(\tilde{\zeta} + \tilde{\eta})\dot{X}_1 + F\cos(\Omega\tau)$.

For the Duffing system with two wells ($s < 0$), an undamped homoclinic orbit $X_{1h}(\tau)$ connects two saddle points $X_1 = \pm\sqrt{|s|}$. Then, for the total energy H without damping, the following holds:

$$H = \frac{1}{2}\dot{X}_1^2 + V(X_1) = 0. \tag{57}$$

Solving Equation (57) yields the analytical expression for the homoclinic orbit:

$$\begin{aligned} X_{1h}(\tau) &= \sqrt{|s|}\tanh\left(\sqrt{\frac{|s|}{2}}\tau\right), \\ \dot{X}_{1h}(\tau) &= \frac{|s|}{\sqrt{2}}\operatorname{sech}^2\left(\sqrt{\frac{|s|}{2}}\tau\right). \end{aligned} \tag{58}$$

Then, the Melnikov function for Equation (47) can be defined as:

$$M(\tau_0) = -\int_{-\infty}^{\infty} \dot{X}_{1h}(\tau)\left[-(\tilde{\zeta} + \tilde{\eta})\dot{X}_{1h}(\tau) + F\cos(\Omega(\tau + \tau_0))\right]\mathrm{d}\tau. \tag{59}$$

Expanding Equation (59) yields:

$$M(\tau_0) = -(\tilde{\zeta} + \tilde{\eta})\underbrace{\int_{-\infty}^{\infty} \left(\dot{X}_{1h}(\tau)\right)^2\mathrm{d}\tau}_{\text{Damping dissipates energy}} + F\underbrace{\int_{-\infty}^{\infty} \dot{X}_{1h}(\tau)\cos(\Omega(\tau + \tau_0))\mathrm{d}\tau.}_{\text{External excitation inputs energy}} \tag{60}$$

where the first and second integrals represent the energy dissipated by damping and the energy input from external excitation, respectively.

Substituting $X_{1h}(\tau)$ from Equation (58) into the damping integral in Equation (60) yields:

$$\int_{-\infty}^{\infty} \left(\dot{X}_{1h}(\tau)\right)^2\mathrm{d}\tau = \int_{-\infty}^{\infty} \frac{|s|^2}{2}\operatorname{sech}^4\left(\sqrt{\frac{|s|}{2}}\tau\right)\mathrm{d}\tau. \tag{61}$$

Let $T = \sqrt{|s|/2}\tau$; then $\mathrm{d}\tau = \sqrt{2/|s|}\mathrm{d}T$, and we obtain:

$$\int_{-\infty}^{\infty} \left(\dot{X}_{1h}(\tau)\right)^2\mathrm{d}\tau = \frac{|s|^2}{2}\sqrt{\frac{2}{|s|}}\int_{-\infty}^{\infty} \operatorname{sech}^4(T)\mathrm{d}T = \frac{|s|^{\frac{3}{2}}}{\sqrt{2}} \cdot \frac{4}{3} = \frac{2\sqrt{2}}{3}|s|^{\frac{3}{2}}. \tag{62}$$

For the external excitation integral in Equation (60), we have:

$$\begin{aligned} \int_{-\infty}^{\infty} \dot{X}_{1h}(\tau)F\cos(\Omega(\tau + \tau_0))\mathrm{d}\tau &= \int_{-\infty}^{\infty} \dot{X}_{1h}(\tau)\cos(\Omega\tau + \Omega\tau_0)\mathrm{d}\tau \\ &= \cos(\Omega\tau_0)\int_{-\infty}^{\infty} \dot{X}_{1h}(\tau)\cos(\Omega\tau)\mathrm{d}\tau, \end{aligned} \tag{63}$$

where:

$$\int_{-\infty}^{\infty} \dot{X}_{1h}(\tau)\cos(\Omega\tau)\mathrm{d}\tau = \pi\mathrm{sech}\left(\frac{\pi\Omega}{2\sqrt{|s|}}\right). \tag{64}$$

Substituting Equations (61) and (64) into Equation (60), chaos occurs when the Melnikov function has a zero:

$$M(\tau_0) = -\left(\tilde{\zeta} + \tilde{\eta}\right)\frac{2\sqrt{2}}{3}|s|^{\frac{3}{2}} + F\pi\mathrm{sech}\left(\frac{\pi\Omega}{2\sqrt{|s|}}\right)\cos(\Omega\tau_0) = 0. \tag{65}$$

For Equation (65), the maximum value occurs when $\cos(\Omega\tau_0) = 1$. In this case, the calculation of the critical excitation corresponds to Equation (48).

Appendix B: Mechanism-based physical indicators

To complement the geometric and frequency-domain analyses, three mechanism-related physical indicators are introduced to reveal the underlying energy flow and coupling behavior of the 2-DOF system. These indicators are evaluated directly from the numerical time histories of the dimensionless responses.

The instantaneous dimensionless total mechanical energy of the coupled system is defined as:

$$E(\tau) = \frac{1}{2}\dot{X}_1^2 + \frac{\gamma}{2}\dot{X}_2^2 + \frac{s}{2}X_1^2 + \frac{1}{4}X_1^4 + \frac{\alpha}{2}(X_1 - X_2)^2, \tag{66}$$

which consists of the kinetic energy of the oscillator and eccentric block, the linear and cubic potential energy of the oscillator, and the coupling spring energy. The time evolution of $E(\tau)$ provides a direct measure of the system's overall vibration intensity and stability.

Since the external excitation is applied to the eccentric block, the instantaneous injected power is given by:

$$P_{in}(\tau) = F\cos(\Omega\tau)\dot{X}_2(\tau). \tag{67}$$

The instantaneous dissipated power due to structural and coupling damping is:

$$P_{diss}(\tau) = 2\zeta\dot{X}_1^2(\tau) + \eta\left(\dot{X}_1(\tau) - \dot{X}_2(\tau)\right)^2. \tag{68}$$

Accordingly, the energy balance for the system satisfies:

$$\frac{\mathrm{d}E}{\mathrm{d}\tau} = P_{in}(\tau) - P_{diss}(\tau), \tag{69}$$

which can be used as a consistency check for numerical integration and, more importantly, provides a physically interpretable basis to assess how excitation and dissipation compete over time.

To quantify the coupling-induced coordination between the oscillator and the eccentric block, instantaneous phases $\phi_1(\tau)$ and $\phi_2(\tau)$ are extracted from $X_1(\tau)$ and $X_2(\tau)$ *via* the Hilbert transform (after removing the mean to avoid DC bias). The instantaneous phase difference is defined as:

$$\Delta\phi(\tau) = \mathrm{wrap}(\phi_1(\tau) - \phi_2(\tau)) \in (-\pi, \pi], \tag{70}$$

and the degree of phase synchronization is quantified by the phase-locking value (PLV):

$$PLV = \left|\left\langle e^{i\Delta\phi(\tau)}\right\rangle\right|, \tag{71}$$

where $\langle\cdot\rangle$ denotes time averaging. A PLV close to unity indicates strong phase locking, whereas smaller values indicate weaker synchronization, which is often associated with quasiperiodic or chaotic responses in coupled nonlinear oscillators.

Appendix C: Computation of the largest Lyapunov exponent (LLE)

The largest Lyapunov exponent (LLE) reported in this study is computed from the numerical time histories of the full 2-DOF system using a standard variational-dynamics approach based on QR re-orthonormalization. The nonlinear state vector is:

$$Z(\tau) = \left[X_1\ \dot{X}_1\ X_2\ \dot{X}_2 \right]^{\mathrm{T}} \in \mathbb{R}^4, \tag{72}$$

and the system is integrated with MATLAB ode45 (Dormand and Prince 1980; Shampine and Reichelt 1997) using relative and absolute tolerances of 10^{-8} and 10^{-9}, respectively, and a maximum step size set to $0.5T_{drive}$ (where $T_{drive} = 2\pi/\Omega$). A transient interval of $100T_{drive}$ is discarded, and the LLE is evaluated on the remaining time window up to $300T_{drive}$.

To compute the local linearization, the Jacobian matrix $A(\tau) = \partial f/\partial Z$ is approximated at each sampled time τ_k by finite differences. Specifically, with a perturbation size $\varepsilon_{FD} = 10^{-8}$, each column of $A(\tau_k)$ is obtained as:

$$A(:,j) \approx \frac{f\left(\tau_k, Z_k + \varepsilon_{FD} e_j\right) - f(\tau_k, Z_k)}{\varepsilon_{FD}}, \tag{73}$$

where e_j is the j-th unit vector and f denotes the right-hand side of the state-space model.

Over a small interval $\Delta\tau$ (taken as the mean sampling time step of the post-transient solution), the state transition matrix of the variational system is approximated by:

$$\Phi_k = \exp\left(A(\tau_k)\Delta\tau\right). \tag{74}$$

The tangent basis is propagated as $Y_k = \Phi_k Q_{k-1}$, followed by QR decomposition $Y_k = Q_k R_k$. The logarithms of the diagonal entries of R_k are accumulated to obtain the Lyapunov spectrum estimates. The LLE is then taken as the maximum component of the spectrum, and its running estimate is recorded as a function of elapsed time to demonstrate convergence. In the implementation, QR re-orthonormalization is performed at every time step (i.e., the renormalization interval equals $\Delta\tau$), and the LLE curve shown in the figures corresponds to this running maximum estimate.